

Specific star formation rates in the $M_{\text{bh}}-M_{*,\text{sph}}$ diagram and the evolutionary pathways of galaxies across the sSFR- M_* diagram

Alister W. Graham^{1*}, T. H. Jarrett², and M. E. Cluver^{1,3}

¹Centre for Astrophysics and Supercomputing, Swinburne University of Technology, Hawthorn, VIC 3122, Australia

²Department of Astronomy, University of Cape Town, Rondebosch, South Africa

³Department of Physics and Astronomy, University of the Western Cape, Robert Sobukwe Road, Bellville, 7535, South Africa

Accepted XXX. Received YYY; in original form ZZZ

ABSTRACT

It has been suggested that the bulge-to-total stellar mass ratio or feedback from black holes (BHs), traced by the BH-to-(total stellar) mass ratio, might establish a galaxy’s specific star formation rate (sSFR). We reveal that a galaxy’s morphology — reflecting its formation history, particularly accretions and mergers — is a far better determinant of the sSFR. Consequently, we suggest that galaxy formation models which regulate the sSFR primarily through BH feedback prescriptions or bulge-regulated disc fragmentation consider acquisitions and mergers which establish the galaxy morphology. We additionally make several new observations regarding current ($z \sim 0$) star-formation rates. (i) Galaxies with little to no star formation have bulges with an extensive range of stellar masses; bulge mass does not dictate presence/absence on the ‘star-forming main sequence’. (ii) The (wet merger)-built, dust-rich S0 galaxies are the ‘green valley’ bridging population between elliptical galaxies on the ‘red sequence’ and spiral galaxies on the blue star-forming main sequence. (iii) The dust-poor S0 galaxies are not on the star-forming main sequence nor in the ‘green valley’. Instead, they wait in the field for gas accretion and/or minor mergers to transform them into spiral galaxies. Mid-infrared sample selection can miss these (primordial) low dust-content and low stellar-luminosity S0 galaxies. Finally, the appearance of the quasi-triangular-shaped galaxy-assembly sequence, previously dubbed the Triangal, which tracks the morphological evolution of galaxies, is revealed in the sSFR-(stellar mass) diagram.

Key words: galaxies: bulges – galaxies: star formation – galaxies: interactions – galaxies: evolution – (galaxies:) quasars: supermassive black holes

1 INTRODUCTION

Positions in the (black hole mass, M_{bh})-(spheroid’s stellar mass, $M_{*,\text{sph}}$) diagram (Kormendy & Richstone 1995; Magorrian et al. 1998; Salucci et al. 2000; Laor 2001) are now known to reflect a galaxy’s morphology and thus the formation processes establishing the galaxies’ morphologies. Savorgnan et al. (2016) introduced the notion of a red and blue sequence in the $M_{\text{bh}}-M_{*,\text{sph}}$ diagram for early-type galaxies (ETGs) and late-type galaxies (LTGs), respectively. The steep blue sequence for LTGs (Davis et al. 2019; Graham & Sahu 2023a) is defined by a near-quadratic or ‘super-quadratic’ relation¹ and the ETG classification has since been considerably refined. Indeed, the well-known near-linear ‘red sequence’ is now recognised as intensely dependent on the sample selection (Sahu et al. 2019; Graham 2023c).

Separating the elliptical (E) galaxies from the lenticular (S0) galaxies² results in $M_{\text{bh}}-M_{*,\text{sph}}$ relations with a logarithmic slope of 1.6–1.9 (Sahu et al. 2019; Graham & Sahu 2023a). Upon making a further distinction between dust-poor and dust-rich S0 galaxies, a galaxy-by-galaxy search of the literature revealed (Graham 2023b, see the references in table 2) that bulk of the latter population were built from major³ ‘wet’ mergers, i.e., gas-rich mergers, while the dust-poor S0 galaxies were not. Both types of S0 galaxy follow their own near-quadratic or super-quadratic $M_{\text{bh}}-M_{*,\text{sph}}$ relation with the galaxy sample size sufficient to reveal substantially different $M_{\text{bh}}/M_{*,\text{sph}}$ ratios at a given spheroid stellar mass (Graham 2023b). Furthermore, the spiral (S) galaxies form a bridging population between the dust-poor and dust-rich S0 galaxies. Moreover, the stellar masses of these disc galaxies and their spheroids

* E-mail: AGraham@swin.edu.au

¹ Graham & Scott (2015, their footnote 14) used the term ‘super-quadratic’ to denote an exponent in a scaling relation between 2 and 3.

² The S0 galaxies in our sample are spirallless galaxies with a substantial, i.e., not just nuclear, disc component.

³ The term ‘major merger’ refers to a roughly equal mass merger event, as opposed to a ‘minor merger’.

suggests that the S galaxies originated from what are now the dust-poor S0 galaxies, likely due to ongoing fuelling and gravitational perturbations from accretions and minor mergers, as discussed in [Graham \(2023c\)](#).

These advances are important for understanding the gravitational wave background ([Arzoumanian et al. 2020](#); [Middleton et al. 2021](#); [Auclair et al. 2022](#)) because the somewhat primordial, dust-poor S0 galaxies ([Sil'chenko 2013](#)) are not built from major mergers involving colliding supermassive black holes (SMBHs). Therefore, they should be excluded (as done in [Graham 2023c](#)) when establishing the $M_{\text{bh}}-M_{*,\text{gal}}$ relation for use in studies of gravitational waves. Furthermore, upon distinguishing between ordinary E galaxies and brightest cluster galaxies (BCGs), they too follow their own separate near-quadratic $M_{\text{bh}}-M_{*,\text{sph}}$ relations with independent normalisation points, i.e., zero-points ([Graham 2023c](#)). The E galaxies are predominantly built from major dry mergers, evinced by the E galaxies' depleted stellar cores ([Begelman et al. 1980](#); [Milosavljević & Merritt 2001](#); [Graham 2004](#)), the (SMBH and spheroid) mass jump when transitioning from the S0 to the E galaxy relations in the $M_{\text{bh}}-M_{*,\text{sph}}$ diagram ([Graham & Sahu 2023a](#); [Graham 2023b](#), section 3.4), plus the presence of shells and multiple nuclei (e.g. [Fort et al. 1986](#); [Lauer 1988](#); [Hernquist & Spergel 1992](#)).

Given these developments, active galactic nuclei (AGN) feedback models producing a near-linear $M_{\text{bh}}-M_{*,\text{gal}}$ relation for (spheroid-dominated) E galaxies appear to be neither accurate (because the E galaxy $M_{\text{bh}}-M_{*,\text{gal}}$ relation has a near-quadratic slope) nor appropriate (because 'dry' mergers, i.e., gas-poor mergers, rather than AGN-regulated star formation, established the E galaxies and their $M_{\text{bh}}-M_{*,\text{gal}}$ and $M_{\text{bh}}-\sigma$ scaling relations, [Graham 2023a](#)). Furthermore, for the spiral (S) galaxies which are undergoing star formation, one observes $M_{\text{bh}} \propto M_{*,\text{gal}}^3$ ([Davis et al. 2018](#); [Graham 2023c](#)), which is steeper than the S galaxy $M_{\text{bh}} \propto M_{*,\text{sph}}^2$ relation due to the systematically larger ratio of galaxy-to-spheroid stellar mass in S galaxies with smaller black holes.

Building on these (galaxy morphology)-dependent relations in the $M_{\text{bh}}-M_{*,\text{sph}}$ and $M_{\text{bh}}-M_{*,\text{gal}}$ diagrams, [Graham \(2023c\)](#) explains the speciation of galaxies, i.e., the transformation between different galaxy types, in terms of accretions and mergers. In this picture, (i) S galaxies grow through accretion and minor mergers onto what were armless disc galaxies (today's dust-poor S0 galaxies), (ii) the gas-rich major merger of S galaxies builds dust-rich S0 galaxies⁴, and (iii) the relatively major dry merger of S0 galaxies with substantial spheroidal-components builds elliptical (ES)⁵ and E galaxies.⁶ Subsequent mergers build what is likely to be the BCGs. At each step in the evolutionary chain, the black hole and spheroid may grow, with an entropy increase that sees pre-existing disc stars on ordered circular orbits become a part of a 'dynamically hot' bulge, aka spheroid. New stars can also form, and the black holes can grow through black hole mergers, consumption of stars, and gas-fuelling.

Previously, with just one recognised type of lenticular galaxy⁷, prior to the realisation that the S galaxies are the bridging popu-

lation between dust-poor and dust-rich S0 galaxies — the above sequence of galactic transformation had not been fully appreciated. [Graham \(2023c\)](#) used the above sequence to modify the galaxy anatomy sequence of Jeans-Reynolds-Lundmark-Hubble ([Jeans 1919](#); [Reynolds 1920](#); [Lundmark 1925](#); [Reynolds 1925](#); [Hubble 1926](#); [Lundmark 1927](#); [Hubble 1936](#)) and also the [van den Bergh \(1976\)](#) Trident and ATLAS^{3D} Comb ([Cappellari et al. 2011](#)). Moreover, [Graham \(2023c\)](#) included evolutionary pathways to produce a quasi-triangular-shaped sequence, referred to as the 'Triangal', that tracks growth in stellar mass, particularly the spheroids' stellar mass.⁸ Here, we report on the presence of this growth sequence in the diagram of specific star formation rate (sSFR) versus stellar mass.

This present work follows [Terrazas et al. \(2016\)](#) and [Terrazas et al. \(2017\)](#), which interpreted the red and blue sequence from [Savorgnan et al. \(2016\)](#) as primarily a consequence of black hole feedback rather than galaxy morphology and, thus, assembly history. Rather than showing the galaxy morphology in the $M_{\text{bh}}-M_{*,\text{gal}}$ diagram, those works presented the sSFR in this diagram. They argued that systems with lower $M_{\text{bh}}/M_{*,\text{gal}}$ ratios are less efficient at shutting down star formation; that is, the AGN feedback was said to be less efficient in galaxies with lower $M_{\text{bh}}/M_{*,\text{gal}}$ ratios, and this explains why such galaxies have a higher sSFR. At face value, this seems plausible, and we investigate if this is the optimal interpretation. We conclude it is not.

We make use of *Wide-field Infrared Survey Explorer (WISE)* ([Wright et al. 2010](#)) data to measure or constrain the SFRs of ~ 100 galaxies with carefully considered (not automated) multicomponent decompositions⁹, refined morphologies¹⁰, and directly measured central black hole masses (Section 2). Given the proximity of the galaxy sample, typically within tens of Mpc, *WISE* can measure intrinsically low levels of dust emission and star formation often missed in surveys. As such, our sample includes some low-mass galaxies with low levels of star formation that are routinely undetected and overlooked by large redshift surveys attempting to capture a representative slice of the Universe. Similarly, morphology "at a distance" can be challenging, so it too tends not to enter the star-formation conversation at a level beyond LTGs versus ETGs. However, these facets prove to be essential for understanding galaxy evolution as a whole and reflect a general need to consider what the nearby Universe can uniquely tell us.

Section 3.1 explores the sSFR as a function of the $M_{\text{bh}}/M_{*,\text{gal}}$ ratio, the $M_{\text{bh}}/M_{*,\text{sph}}$ ratio, and the galaxy morphology. While a broad trend between sSFR and $M_{\text{bh}}/M_{*,\text{gal}}$ is apparent, the sSFR much more closely tracks the galaxy morphology. Similarly, while a trend between sSFR and $M_{*,\text{sph}}/M_{*,\text{gal}}$, i.e., spheroid-to-total stellar mass ratio, is also evident — as seen in [Martig et al. \(2009\)](#) — the primary connection again appears to be between the sSFR and the galaxy morphology. Various sSFR- M_* diagrams are presented in Section 3.2, and the appearance of the 'Triangal' ([Graham 2023c](#)) is revealed in the sSFR- $M_{*,\text{gal}}$ diagram. A summary is provided in Section 4.

galaxies need not contain a bulge component (e.g., [van den Bergh 1976](#)), although all in our sample do.

⁸ [Graham & Sahu \(2023b\)](#) discuss 'non-growth' pathways which either halt star formation and turn S galaxies into gas-poor S0 galaxies (e.g., [Spitzer & Baade 1951](#); [Gunn & Gott 1972](#)) or strip stars to produce smaller galaxies (e.g., [Moore et al. 1996](#); [Bekki et al. 2001](#)).

⁹ These are superior to two-component [Sérsic \(1963\)](#) bulge plus exponential disc ([Patterson 1940](#)) decompositions.

¹⁰ Many S0 galaxies were previously mislabelled as E galaxies.

⁴ One may expect a high fraction of quasar AGN in these dust-rich S0 galaxies when they are built.

⁵ [Liller \(1966\)](#) introduced the ES galaxy notation for ETGs with an intermediate-scale disc fully embedded within their spheroid.

⁶ These E galaxies built from relatively major dry mergers may not display a substantial AGN.

⁷ ([Reynolds 1925](#)) introduced the spiralless disc galaxy type as a bridge between E and S galaxy types. As with the S galaxies, the low-mass S0

2 DATA

2.1 The galaxy/SMBH sample

The galaxy sample consists of 103 galaxies with directly measured SMBH masses (tabulated in [Graham & Sahu 2023a](#)) and multicomponent decompositions of Spitzer Space Telescope (SST; [Werner et al. 2004](#); [Fazio et al. 2004](#)) $3.6\ \mu\text{m}$ images. Rather than automated fits of 2, 3, or 4 [Sérsic \(1963\)](#) $R^{1/n}$ functions, the decompositions were based on physical components such as bars (fit with a Ferrer function), rings (Gaussian function), bulges (Sérsic function), inner and outer discs (truncated, anti-truncated, and unbroken exponential function), and more. The stellar masses of the spheroids used in the figures pertain to either the bulge component, when present, of the disc galaxies or (practically) the bulk of an elliptical galaxy modulo small nuclear discs when present. That is, bars and inner discs do not enter into the spheroid mass. References to updated galaxy distances — used for the SMBH masses and absolute magnitudes — are provided in [Graham & Sahu \(2023a, their Table 1\)](#), as are references for where the decomposition of each galaxy can be seen. These references also successively note from where the original SMBH masses were taken. Galaxy model magnitudes were built from the sum of the galaxy component magnitudes and agreed (<0.02 mag) with direct integration of the light profile.

Among the disc galaxies, i.e., the S and S0 galaxies, their spheroids display a continuous trend between Sérsic index n , a measure of the radial concentration of their stars ([Trujillo et al. 2001](#); [Graham & Driver 2005](#)), and the stellar luminosity/mass ([Sahu et al. 2020](#); [Hon et al. 2023](#)). These spheroids are distinct from inner discs and (peanut shell)-shaped structures (e.g., [de Vaucouleurs & de Vaucouleurs 1972](#); [Jarvis 1986](#); [Ciambur & Graham 2016](#)). In our data set, inner discs were modelled as such and (peanut shell)-shaped structures were either modelled (e.g., [Davis et al. 2019](#); [Sahu et al. 2019](#)) as separate components, e.g., lenses ([Buta et al. 2006](#)) or effectively folded back into the bar component from which they emerged ([Hohl 1975](#); [Combes & Sanders 1981](#); [Athanassoula 2005](#); [Saha et al. 2018](#)). This modelling was performed using an isophotal analysis technique ([Carter 1978](#)) that measured the radially-varying Fourier harmonic terms that describe the isophote’s deviations from ellipses due to, for example, buckled bars. The corrected version ([Ciambur 2015](#)) of the ELLIPSE task ([Jedrzejewski 1987](#)) in the Image Reduction and Analysis Facility (IRAF) was used to extract the (desired) symmetrical component of the two-dimensional galaxy image. This has the added benefit of leaving the non-symmetrical disturbances in the residual image for further analysis, such as, for example, the discovery of the shredded galaxy *Nikhuli* ([Graham et al. 2021](#)), and preventing such features from biasing the image decomposition into regular/standard components. The spheroids were modelled with the [Sérsic \(1963\)](#) $R^{1/n}$ function described in ([Graham & Driver 2005](#)). Further details of the spheroid extraction process are provided in [Savorgnan & Graham \(2016a\)](#), [Davis et al. \(2019\)](#), [Sahu et al. \(2019\)](#), and [Graham & Sahu \(2023b\)](#).

Stemming from the decompositions of the galaxy images — which were supported by recourse to kinematic profiles and maps, often revealing the presence of rotating discs in ETGs — came knowledge of the galaxy morphologies: spiral, lenticular, and elliptical. From cursory (qualitative) inspection of images, discs in ETGs are notoriously hard to spot and, as discussed in [Graham \(2019\)](#), and references therein, have often been missed. For example, *Fornax A* was historically classified as an E galaxy, but [Searle \(1965\)](#) and [de Vaucouleurs et al. \(1991\)](#) designated it a peculiar

S0 galaxy with a disc and [D’Onofrio et al. \(1995\)](#) presented the rotation of the galaxy’s stars. Therefore, established quantitative measures of the images were used to detect the presence and quantify the extent of the galaxies’ discs. While a qualitative judgement on the presence of a spiral was initially performed, a quantitative analysis of most of the spirals can be found in [Davis et al. \(2017\)](#). Due to the proximity of the galaxies, there was little ambiguity at to whether a galaxy was a spiral galaxy or not. Although weak spiral patterns can exist (e.g., [Jerjen et al. 2000](#); [Graham et al. 2003](#)), there is nothing controversial with our designation of the spiral galaxies, in that it agrees with decades of literature. Furthermore, no weak spirals were discovered in the residual (galaxy minus model) images. The only point worthy of note is that here, as in ([Graham 2023b](#)), NGC 2974 (aka NGC 2652) and NGC 4594 (the *Sombrero* galaxy) are regarded as S0 rather than S galaxies.

To be clear, galaxies identified as having large-scale discs, i.e., discs that dominate the light at large radii but have no spiral pattern, are denoted as S0 galaxies. The S0 galaxies are invariably ‘fast rotators,’ as revealed through kinematic profiles and maps available in the literature. No recourse to star formation rates was used to identify any galaxy’s morphological type or the ‘dust bins’ (see later) for the S0 galaxies. No recourse to clumpiness, small-scale or otherwise, was used to establish the galaxies’ morphological types. While some S0 galaxies have a smooth appearance — which has, in part, led to some past misidentifications as E galaxies — other S0 galaxies appear relatively clumpy at optical wavelengths (e.g., NGC 524, *Fornax A*, *Centaurus A*). As such, (wavelength-dependent) clumpiness should be interpreted with care in the $s\text{SFR}-M_*$ diagram as it may not have the same finesse as the morphological type. The ES galaxies ([Liller 1966](#); [Graham 2019](#)), found to have spirallike intermediate-scale discs, i.e., discs that do not dominate the light at large radii, are tabulated in [Graham & Sahu \(2023b\)](#), as were the cD and BCGs. The elliptical galaxies, of course, have neither a large-scale nor an intermediate-scale disc.

The dust-poor versus dust-rich S0 galaxies were readily identified from a visual inspection of optical images, as reported in [Graham \(2023b\)](#), with most of the dust-rich S0 galaxies individually recognised in the literature as having been built from major gas-rich mergers involving S galaxies. These morphological types are used in the present analysis to help understand the distribution of $s\text{SFRs}$ in the $M_{\text{bh}}-M_{*,\text{sph}}$ diagram and the $s\text{SFR}-M_{*,\text{sph}}$ and $s\text{SFR}-M_{*,\text{gal}}$ diagrams. Conceivably, the build-up (in the disc galaxies) and then the decline (in the E galaxies) of the specific dust mass could also be used. We do not, however, have this measure.

Investigating the lenticular galaxies, [Graham \(2023b\)](#) established four ‘dust bins’ based upon a personal inspection of Hubble Space Telescope images. The bins were denoted with the following codes:

- N for no visible signs of dust;
- n for not much other than a nuclear dust ring/disc;
- y for a weak/mild level of widespread dust; and
- Y for lots of clearly visible widespread dust, i.e. dust-rich.

Examples can be seen in figure 1 of [Graham \(2023b\)](#). Once galaxies become massive, as in the case of the E and ES,e galaxies, they are known to establish hot X-ray emitting halos of gas which effectively destroy the dust grains and eliminate the cold gas enclaves for dust ([Draine & Salpeter 1979](#); [Benson et al. 2003](#); [Galliano et al. 2021](#)). Among the sample of 37 E and ES,e galaxies, including the BCG matching this description, only three are dust-rich (dust bin = Y), while 19 have no visible dust, 8 have only a nuclear dust disc, and 7 have only faint traces of dust beyond their nucleus.

Two of the 103 galaxies (NGC 4395 and NGC 6926) are bulge-less and, as such, only appear in diagrams showing the disc or galaxy stellar mass and not in diagrams showing the bulges' stellar mass.¹¹ Additional notes about the galaxies labelled in some figures are provided in Appendix A.

2.2 Stellar masses

Graham & Sahu (2023a) tabulates the spheroid and galaxy stellar masses, along with the SMBH masses, for the sample. The stellar masses were obtained using the Spitzer 3.6 μm galaxy model magnitudes and colour-dependent (stellar mass)-to-light ratios based on realistic dusty models created by Into & Portinari (2013) for “samples that include a range of morphologies, intrinsic colours and random inclinations”. The $M_*/L_{3.6}$ ratios¹² are around 0.45 for the LTGs and 0.7–0.9 for the ETGs (Graham & Sahu 2023a, their figure 1), and the stellar masses were adjusted to the Kroupa (2002) initial mass function (IMF).

Jarrett et al. (2023) present an alternate prescription to derive stellar masses based on W1 (3.4 μm) ‘total flux’ photometry and colours from *WISE*. This approach was applied to the galaxy sample, many of which were already included in Jarrett et al. (2019). These stellar masses were derived using a Chabrier (2003) IMF. Subtracting 0.05 dex from these *WISE*-based masses effectively converts them to the Kroupa (2002) IMF (Bernardi et al. 2010, their table 2).

Fig. 1 compares the *WISE*- and *SST*-based stellar masses mentioned above. They are seen to differ by roughly a factor of two. The offset has been approximated by the relation

$$\log(M_{\text{SST}}/M_{\odot}) = (6/5.55)[\log(M_{\text{WISE}}/M_{\odot}) - 7] + 7. \quad (1)$$

Such offsets have been seen before, e.g., by Roediger & Courteau (2015, their figure 7), Graham et al. (2019, their figure 4), and Sahu et al. (2019, their figure 4). They can stem from many issues, including the adopted stellar population model and, at infrared wavelengths, the correction for dust glow. Some differences in stellar mass can have their origin in the use of aperture photometry versus extrapolated model photometry from, for example, a single Sérsic $R^{1/n}$ fit or a two-component Sérsic $R^{1/n}$ -bulge plus exponential-disc fit. As Sahu et al. (2023) revealed, it is crucial to be aware of such offsets when applying the $M_{\text{bh}}-M_{*,\text{sph}}$ and $M_{\text{bh}}-M_{*,\text{gal}}$ relations to galaxy samples whose stellar masses may have been inconsistently measured. Differences in the derivation of the stellar mass between samples led to the incorrect suspicion (Shankar et al. 2016) that ETGs with directly measured black hole masses are offset from the ETG population at large in the $M_{*,\text{gal}}$ -(stellar velocity dispersion, σ) diagram. For the current analysis, we do not need to track down the cause(s) of the difference observed in Fig. 1. Nonetheless, it is noted that it primarily arises due to the adopted M/L ratio. Unless otherwise specified, we proceed using the stellar masses from Graham & Sahu (2023a), upon which the black hole scaling relations were previously derived.

2.3 Star Formation Rates

The level of star formation activity in the past 100 Myr is assessed through the infrared emission as measured using the *WISE* total

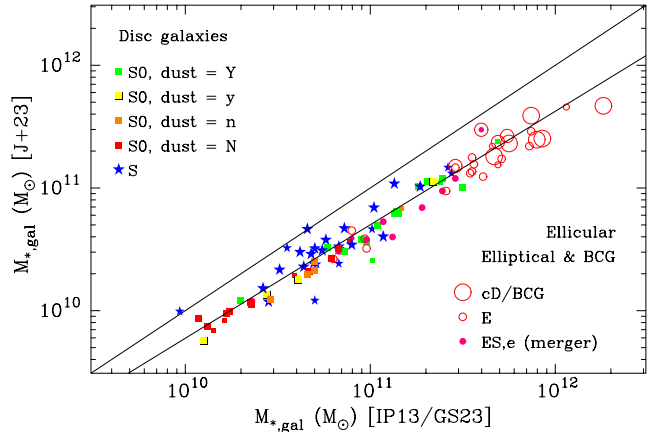


Figure 1. Comparison of the galaxy stellar masses from (i) multicomponent fits to *SST* 3.6 μm imaging data (Graham & Sahu 2023a, their table 1) and using a slight modification of a stellar population model from Into & Portinari (2013), and (ii) a derivation based on *WISE* photometry (Jarrett et al. 2023) after adjusting from a Chabrier (2003) IMF to a Kroupa (2002) IMF (see Table C1). The line through the data is given by Eq. 1.

integrated fluxes and the calibration developed by Cluver et al. (2017, 2023 in preparation), which shows that the 12 and 23 μm mid-infrared bands of *WISE* are an effective predictor of the total infrared luminosity. Half a dozen example galaxy images from *WISE* are shown in Fig. 2. The selection of these six will make sense upon reading Appendix B. The mid-IR is a robust tracer of the dust-obscured star formation activity, but less so with lower mass galaxies that tend to be more dust-free and metal-poor. Cluver et al. (in preparation) have created a UV-based correction to this regime, generally applicable to dwarf galaxies, $\log(M_*/M_{\odot}) < 10$ dex, which accounts for the lower dust opacity and hence, can be used to estimate the total SFR. However, this is only relevant to one galaxy in the sample.

The SFR ($M_{\odot} \text{ year}^{-1}$) is derived from the mid-infrared spectral (νL_{ν}) luminosity, as measured in the *WISE* W3 (12 μm) and W4 (23 μm) imaging bands after subtracting the stellar continuum (inferred from the W1 integrated flux: Cluver et al. 2017; Jarrett et al. 2019). Cluver et al. (in preparation) provide the scaling relations between the mid-IR luminosities and the total infrared luminosity (LTIR), updated from Cluver et al. (2017), which is then converted to the SFR using Calzetti (2013). The mid-IR SFR is then a combination of the inverse-variance weighted W3 and W4 SFRs to derive the optimal SFR traced by the *WISE* mid-IR bands. In this paper, the SFRs for the sample galaxies are compared to their host stellar mass using the galaxy ‘main-sequence’ diagram: global SFR vs mass. A useful variation of this diagram uses the sSFR to gauge the rate at which galaxies are building their disc/bulge (relative to past star formation), for example, Salim et al. (2018).

In Fig. 3, the SFR for the dust-rich S0 galaxies is shown against the *WISE*-based galaxy stellar mass (Jarrett et al. 2023). The bulk of the dust-rich S0 galaxies can be seen to occupy the region for ETGs below the ‘main sequence’ (magenta curve) that normal, star-forming galaxies tend to occupy given their global (past-to-present) stellar mass. However, they do not simply cluster about the high-density region of the red cloud/sequence centered at $\log(M_{*,\text{gal}}/M_{\odot}) \sim 11$ dex and $\log(\text{SFR } M_{\odot} \text{ yr}^{-1}) \sim -1$ dex, where the E/ES,e galaxies will later be shown to reside.

Not all of the galaxies in the sample are detected in *WISE*’s W3

¹¹ The terms bulge and spheroid are used interchangeably in this article.

¹² The $M_*/L_{2.2}$ expression in Into & Portinari (2013) was converted to $M_*/L_{3.6}$ in equation 2 in Graham & Sahu (2023a).

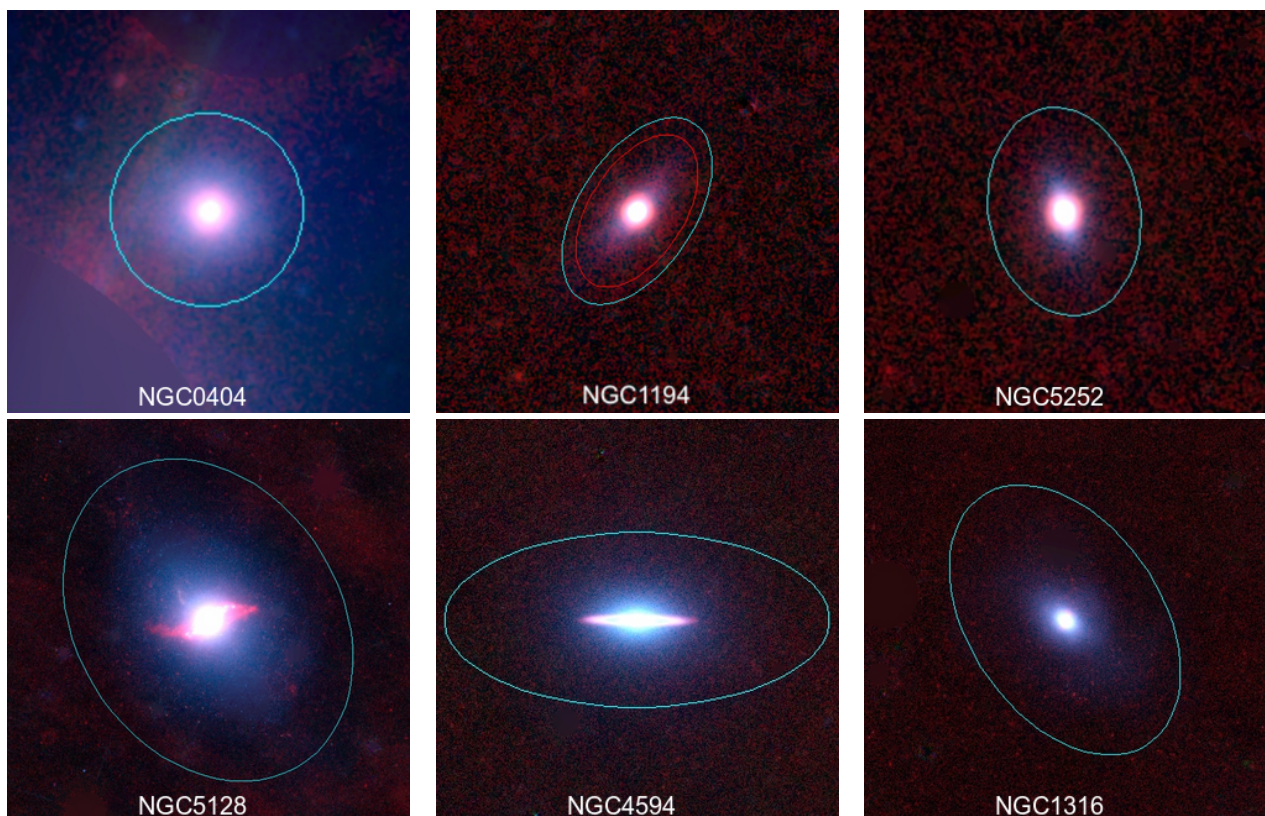


Figure 2. *WISE* 3-colour (W1, W2 and W3 bands) cutouts of select galaxies, after the photometry pipeline has removed foreground stars, background galaxies and other corrections to achieve a cleaner field for analysis. The ellipse denotes the photometric aperture to extract the isophotal flux, roughly 23 mag arcsec⁻² (Vega) in W1 surface brightness. This isophote represents the 1-sigma extent of the galaxy. Total galaxy luminosities were obtained by going beyond this aperture, using a double-Sérsic model.

or W4 bands, notably after the stellar continuum contribution has been subtracted from the integrated fluxes. From the 103 galaxies, we were unable to measure an SFR, or rather, we only have upper-limit measurements for one ES,e galaxy, five dust-poor (dust=N) S0 galaxies, and 14 E galaxies. While this is good, we can turn this statement around to report that 9 of 10 ES,e and 9 of 14 dust-poor (dust=N) S0 galaxies, plus 11 of 25 E galaxies, show up with a non-zero SFR. As revealed in the figures, the associated sSFR rates are at the low level of $10^{-13} \lesssim M_{\odot}\text{yr}^{-1} \lesssim 10^{-12}$.

In passing, it is noted, albeit with a sample of just four ES,b galaxies (treated herein as S0 galaxies), that the ES,b galaxies overlap with the ES,e elliptical galaxies in the sSFR vs $M_{*,\text{galaxy}}$ diagram.

It is also observed that the E galaxy IC 4296 has an undigested component, i.e., a captured galaxy, containing 4.5 per cent of the total stellar mass (Sahu et al. 2019). The past merger giving rise to this component may have induced some star formation, as IC 4296 has a sSFR of -12.74 dex. The E galaxy NGC 4261 may also contain an undigested component, perhaps explaining why it has an sSFR of -12.36 dex. However, there are nine other E galaxies with a non-zero SFR for which our galaxy decomposition did not require the inclusion of such a component. It could be that such yet-to-be-assimilated components are (now) small enough not to require modelling. Alternatively, the low sSFRs may be suggesting that something more is afoot, influencing the measurement. These galaxies may have some very low levels of warm dust emission heated by old stars — with the dust coming from stellar winds (e.g., Gail & Sedlmayr 1988; Chieffi & Limongi 2004) and supernovae

(e.g., Todini & Ferrara 2001; Limongi & Chieffi 2003; Matsuura et al. 2011) — as opposed to heating from recent (~ 100 Myr) star-formation. This emission is typically negligible relative to young-disc star formation emission but may be appreciable for the stellar-dominated (i.e., bulge) components of ETGs (Jarrett et al. 2019). We therefore caution that some of the *WISE* SFRs are likely overestimated and may serve best as upper limits.

2.3.1 Active Galactic Nuclei

Star formation activity is inferred from the continuum-subtracted *WISE* luminosity. The underlying assumption is that the infrared emission arises from interstellar medium dust/molecules heated by UV radiation from recent star formation. Complications arise from dust opacity and metallicity (as noted above), dust heating from old stars (unrelated to recent star formation), and active galactic nuclei, whose dusty torus emission may be powerful enough to compete with or even overwhelm the host galaxy emission. As measured in mid-IR, the galaxy colours may be used to detect dust-obscured AGN emission contaminating the star formation tracers (Jarrett et al. 2011, 2019; Yao et al. 2022).

A couple of galaxies should be, and are, disregarded due to dust-heating from their AGN: they are NGC 1275 and the Circinus galaxy. They have artificially high sSFRs, evident in later figures. Among the 17 dust-rich S0 galaxies (dust=Y), a few appear to have elevated SFRs, placing them on the star-forming main sequence, as

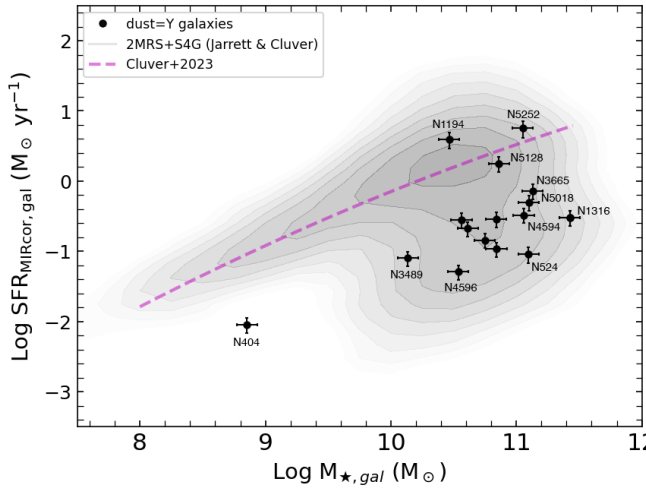


Figure 3. Star formation rate based on *WISE* mid-infrared measurements calibrated to the total infrared luminosity (Cluver+2023 = Cluver et al. in preparation) versus the *WISE*-based stellar mass. The SFRs, given in preparation, are shown here for just the dust-rich E/S0 galaxies in the dust bin ‘dust=Y’. They do not simply cluster about the high density centre of the red sequence/cloud. The relative location of the dust-poor S0 and other galaxy types will be seen in later figures. To cover the region occupied by normal galaxies (Jarrett et al. in preparation), the contours pertain to a larger redshift-zero sample that includes the 2MASS Redshift Survey (2MRS) and Spitzer Survey of Stellar Structure in Galaxies (S⁴G). The magenta line represents the ‘main sequence’ as derived by Cluver et al. (in preparation) using the combined S⁴G and 2MRS samples.

seen in Fig. 3. None of the four dust=y S0 galaxies reside above this main sequence.

Fig. 4 shows the *WISE* W1–W2 colour versus the W2–W3 colour for these dust-rich (dust=Y) S0 galaxies. A relatively red W1–W2 colour (top-side of the diagram) is a signature of AGN heating dominating the global mid-infrared fluxes. It is problematic because it can elevate the inferred SFR. This is, however, not responsible for the bulk of the S0 galaxies with low-to-moderate SFRs. They reside below the main sequence of star formation, delineated by the magenta curve in Fig. 3. Some reside in the so-called ‘green valley’, between this blue sequence of star-forming galaxies and the red cloud/sequence occupied by passive galaxies. Apart from NGC 1194 and NGC 5252, both of which appear to harbour dust-obscured AGN, the dust-rich S0 galaxies do not have colours suggestive of a warm AGN component or a QSO with $(W1-W2) > 0.4$ mag. None of the other S0 galaxies contains a warm AGN. This means that the SFRs are reliable and unlikely a result of AGN-heating of the dust (e.g., Scoville et al. 2000; Kirkpatrick et al. 2015).

It is noted that in the past, the entire star-forming main sequence was more active, with 20 times more star formation at a redshift of 1 and 40 times more at $z = 4$ (Tasca et al. 2015), see also (Bunker et al. 2004; Maraston et al. 2010; Curti et al. 2023; Popesso et al. 2023; Robertson et al. 2023). It is unsurprising to find AGN activity in gas-rich mergers, which may indicate how recently a disturbance or merger occurred. Indeed, due to angular-momentum-zapping gravitational tidal forces sending gas inward to fuel the central black hole(s), the dusty S0 galaxies likely contained quasars (e.g., Hopkins et al. 2008) and may have briefly become ‘starbursts’ and ultraluminous IR galaxies (ULIRGs) with sSFR

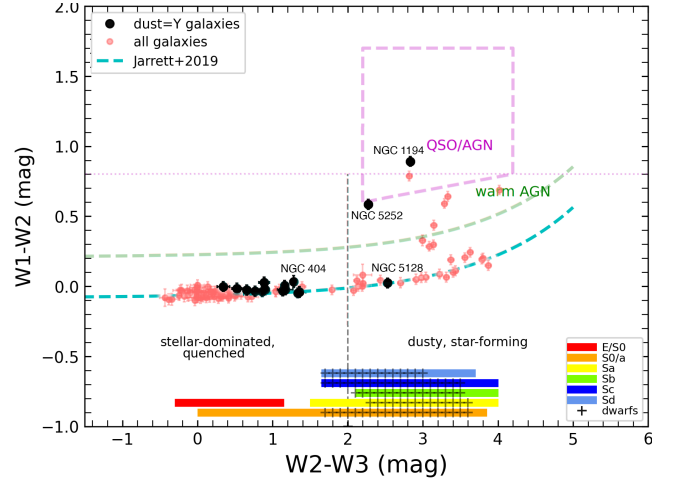


Figure 4. *WISE* colour-colour plot for ‘all’ galaxies (red points). The S0 galaxies with dust=Y are highlighted (black points). All colours are tabulated in Appendix C. NGC 1194 and NGC 5252 are Seyferts with warm W1–W2 colours. Although NGC 5128 (Cen A) is particularly dusty in the central region, its total host galaxy colour is nominal (see also Fig. 2). The diagram indicates where normal star-forming galaxies are expected to lie (dashed thick cyan curve from Jarrett+2019 = Jarrett et al. 2019), with most dusty ETGs on the left and active star-forming galaxies on the right. Five spiral galaxies (Circinus, NGC 1320, NGC 4151, NGC 4388, and NGC 7582) appear above the dashed thin green curve for AGN, with three galaxies (NGC 1275, NGC 2273, and NGC 3227) just below it. Vertical deviations indicate ‘warm’ colours, typically associated with AGN activity, at low levels (see green dashed curve) and where the AGN dominates the total emission (magenta dashed box and dotted line).

$> 10^{-9} M_{\odot} \text{ yr}^{-1}$ when they first formed (Mihos et al. 1992). In the distant past, when today’s dust-poor S0 galaxies were forming on the star-forming sequence, a collision between two of them would also have led to a starburst and perhaps a ULIRG if high-angular-momentum gas reservoirs were brought into play.

In Appendix B, we continue the discussion about AGN with information on individual galaxies.

3 ANALYSIS AND DISCUSSION

3.1 Part 1: SFRs, AGN feedback, and galaxy morphology in the $M_{\text{bh}}-M_{*,\text{sph}}$ diagram

Fig. 5 presents an enhanced view of the galaxy-morphology-dependent $M_{\text{bh}}-M_{*,\text{sph}}$ diagram, previously shown in terms of E, S0 and S galaxies (Savorgnan et al. 2016; Sahu et al. 2019). The broad and roughly quadratic trend seen at $M_{*,\text{sph}} \lesssim 10^{11} M_{\odot}$ for the ensemble of disc galaxies (S galaxies and dust-rich and dust-poor S0 galaxies) was highlighted a decade ago by separating off the E galaxies (built from dry mergers and) possessing cores depleted of stars due to binary SMBHs (Graham 2012; Graham & Scott 2013; Scott et al. 2013). Following Terrazas et al. (2016), see also Terrazas et al. (2017), the right-hand panel of Fig. 5 displays the sSFRs (Section 2.3). It is apparent that the S galaxies have the highest sSFRs, followed by the dust-rich S0 galaxies. The dust-poor S0 and E galaxies (including ES,e and BCG) have low to no detectable sSFR.

Terrazas et al. (2016) suggested that the $M_{\text{bh}}/M_{*,\text{gal}}$ mass ratio dictates the strength of the AGN feedback and, in turn, regulates the sSFR through quenching. To help visualise this scenario,

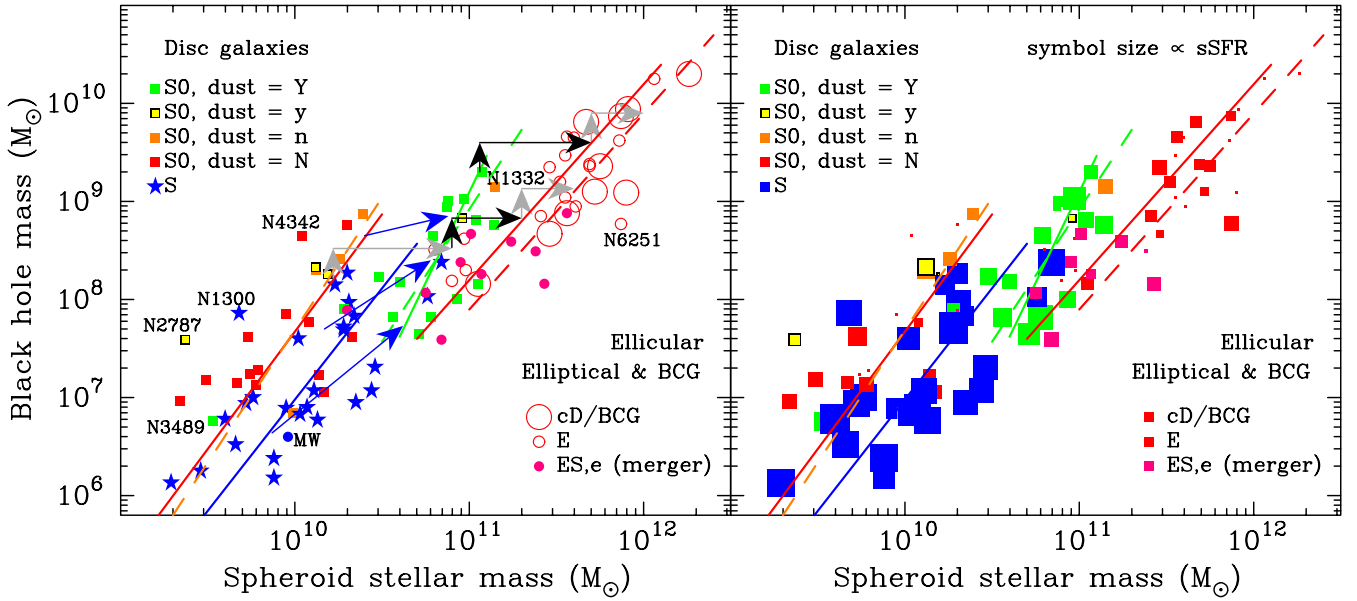


Figure 5. Left: $M_{\text{bh}}-M_{*,\text{sph}}$ diagram as a function of galaxy morphology (figure taken from [Graham 2023c](#)). The red solid line pertains to E and ES,e galaxies, while the red dashed line is representative of the cD and BCGs. Right: $M_{\text{bh}}-M_{*,\text{sph}}$ diagram as a function of galaxy $\text{sSFR}_{*,\text{galaxy}}$. Here, the symbol size reflects the logarithmic value of $\text{sSFR}_{*,\text{galaxy}}$. Only Circinus (S) and NGC 1275 (E) have been excluded from the figure, given how their AGN-heated dust inflates their measured sSFR — see Fig. 8. As explained in [Graham \(2023c\)](#), the labelled galaxies are shown but excluded from the Bayesian regression analyses performed there. Theories for the emergence of spiral patterns in galaxy discs, and evidence of accretion and (bulge-building) minor mergers in S galaxies, is noted in [Graham \(2023c\)](#). The dust-rich S0 galaxies are recognised major wet merger products while the E galaxies, typically with depleted cores, are major dry merger remnants ([Graham 2023b](#)). At a fixed M_{bh} , both $M_{*,\text{sph}}$ and $M_{*,\text{gal}}$ ([Graham 2023c](#), appendix fig. A4) in dust-poor S0 galaxies are lower than that in S galaxies, disfavours the faded/transformed S origin for most dust-poor S0 galaxies.

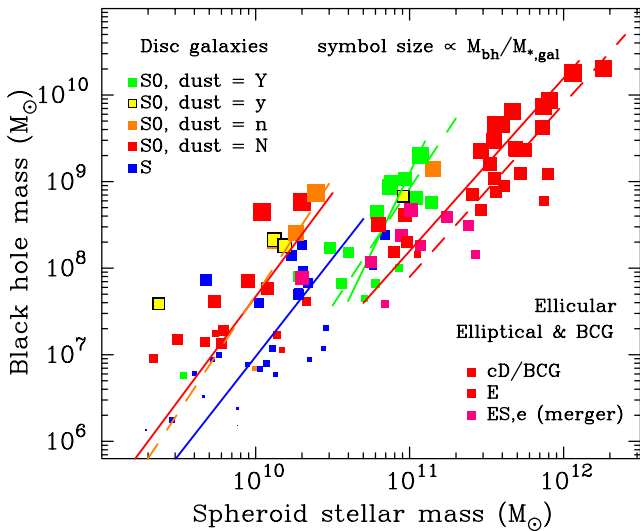


Figure 6. Similar to the right-hand panel of Fig. 5, but here the symbol size represents the $M_{\text{bh}}/M_{*,\text{gal}}$ mass ratio, previously claimed to be regulating the sSFR ([Terrazas et al. 2016](#)). This is tested in Fig. 7 against the notion that the galaxy morphology, reflective of the galaxy accretion/merger history, is the driving force.

Fig. 6 displays the $M_{\text{bh}}/M_{*,\text{gal}}$ mass ratio instead of the sSFR seen in Fig. 5. Two patterns are evident. As one moves down the (galaxy morphology)-dependent sequences to lower masses, the $M_{\text{bh}}/M_{*,\text{gal}}$

ratio decreases. This is as expected given the near-quadratic slope of these $M_{\text{bh}}-M_{*,\text{sph}}$ relations and the equal or steeper $M_{\text{bh}}-M_{*,\text{gal}}$ relations ([Graham 2023c](#)). The second trend is the reduced $M_{\text{bh}}/M_{*,\text{gal}}$ ratio at fixed BH mass as one moves to higher $M_{*,\text{sph}}$. By definition, this is expected for the E galaxies in which $M_{*,\text{sph}} \approx M_{*,\text{gal}}$. For the disc galaxies, it is simply a case of more massive spheroids with the same black hole mass being associated with more massive galaxies.

Modulo a suspected sample selection bias which has missed low-mass BHs in low-stellar-mass, low central surface brightness, dust-poor S0 galaxies, Fig. 7a reveals a trend of decreasing sSFR with increasing ‘specific BH mass’, $M_{\text{bh}}/M_{*,\text{gal}}$. This trend was reported by [Terrazas et al. \(2017\)](#) and is seen in Fig. 6. Multiplying both axes by $M_{*,\text{gal}}$ in Fig. 7a gives an identical trend of decreasing SFR with increasing BH mass. This behaviour is, therefore, understood because elliptical galaxies — built from the merger of disc-dominated galaxies — have larger BH masses and lower star formation rates than spiral galaxies. The future inclusion of low-stellar-mass ETGs with $M_{\text{bh}} \sim 10^{6\pm 1}$ is anticipated to alter this trend. Extrapolating the $M_{\text{bh}}-M_{*,\text{gal}}$ trends seen in [Graham \(2023c](#), figure A4), these disc-dominated low-mass ETGs with low SFR would extend the shelf of dust-poor galaxies (coded orange and red) in Fig. 7 to lower $M_{\text{bh}}/M_{*,\text{gal}}$ ratios, thereby reducing the strength of the correlations seen there.

[Terrazas et al. \(2017\)](#) interpreted the observed trend as indicating a suppression of the sSFR due to greater AGN feedback in systems with higher specific BH masses or, equivalently, a decreased SFR in systems with more massive black holes due to increased AGN feedback. However, and this is the key, Fig. 7 reveals that the $\text{sSFR}_{*,\text{galaxy}}$ correlates better with the galaxy morphology than it does with either of the BH-to-stellar mass ratios

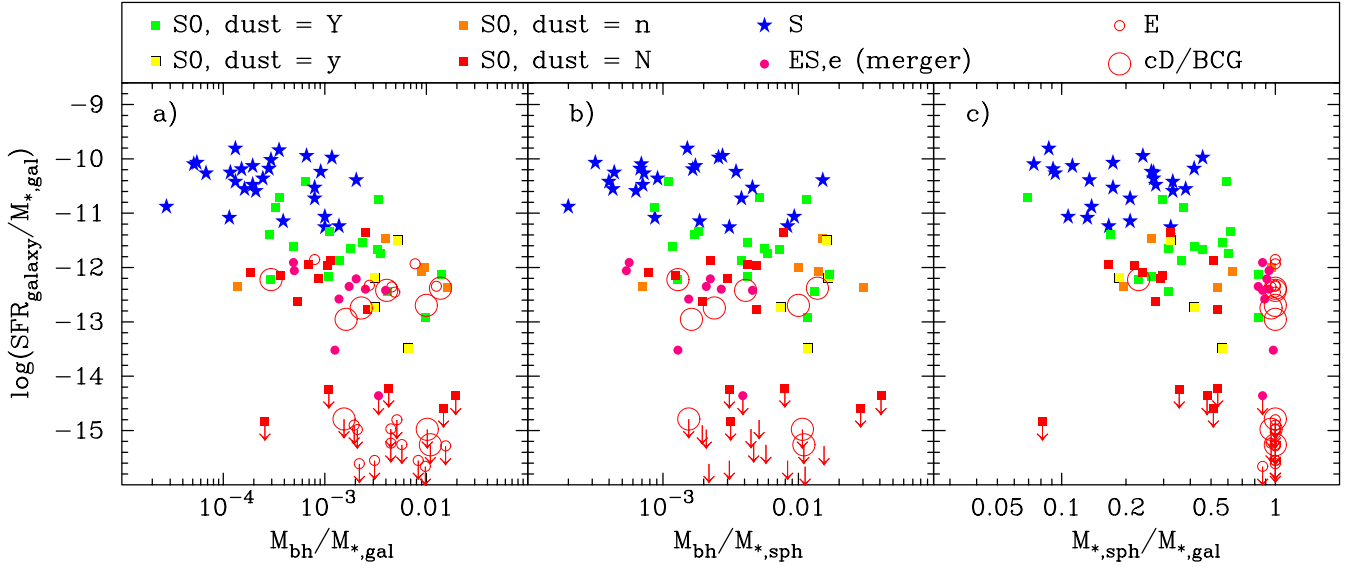


Figure 7. Galaxy specific-SFR versus a) specific black hole mass (left-hand panel), b) $M_{\text{bh}}/M_{*,\text{sph}}$ (middle panel), and c) $M_{*,\text{sph}}/M_{*,\text{gal}}$ (right-hand panel). Note that the trend in the left-hand panel is equivalent to that in the SFR versus black hole mass diagram. It is apparent that the SFR correlates better with the galaxy morphology than the BH-to-stellar mass ratio or the bulge-to-total stellar mass ratio (right-hand panel). Circinus and NGC 1275 have been excluded from the figure for clarity, given that their AGN-heated dust inflates the measured sSFR. Low-mass dust-poor S0 galaxies have low central surface brightness and are likely missing from the lower left due to sample selection.

shown there, as is evident from the scatter at fixed $M_{\text{bh}}/M_{*,\text{gal}}$ or $M_{\text{bh}}/M_{*,\text{sph}}$. That is, Fig. 7 reveals that the sSFR cares more about the galaxy morphology, which reflects the galaxy formation history, than the $M_{\text{bh}}/M_{*,\text{gal}}$ (or $M_{\text{bh}}/M_{*,\text{sph}}$, Fig. 7b) ratio. In other words, ($M_{\text{bh}}/M_{*,\text{gal}}$)-dependent AGN feedback is not the driving force regulating the SFRs in galaxies. Accretions and mergers, which set the morphology, are more critical.

A consequence of this result is that galaxy formation models should not tune the sSFR primarily through prescriptions of black hole feedback tied to the $M_{\text{bh}}/M_{*,\text{gal}}$ ratio but rather through (gas-rich/poor) accretion events and mergers which dictate the galaxies morphologies (Graham 2023c), coupled with, of course, gas recycling from stellar winds (e.g., Martig & Bournaud 2010).

Fig. 7c reveals that while the sSFR correlates more tightly with the bulge-to-total, B/T , stellar mass ratio, $M_{*,\text{sph}}/M_{*,\text{gal}}$, than the BH-to-stellar mass ratios (using either $M_{*,\text{sph}}$ or $M_{*,\text{gal}}$), the B/T ratio is also not the driving force.¹³ For example, dust-poor ETGs with $0.15 < B/T < 0.4$ have $-12 \lesssim sSFR_{*,\text{galaxy}} \lesssim -13$ dex, while LTGs with the same B/T ratios have $-10 \lesssim sSFR_{*,\text{galaxy}} \lesssim -11$ dex. This observation would appear to be at odds with the idea that a bigger (relative to the disc) bulge prevents star formation by stabilising the disc (e.g., Martig et al. 2009). While we do not rule out that this may occur at some level, and it is again noted that inner discs, bars and (peanut-shell)-shaped structures are excluded from our ‘bulge’ mass, there appears to be a bigger factor at play. Specifically, the galaxy morphology, a tracer of the accretion and merger history, seems to dominate in setting the sSFR.

¹³ The same finding is reached when using the bulge-to-disc, $B/D = [(B/T)^{-1} - 1]^{-1}$, stellar mass ratio, $M_{*,\text{sph}}/M_{*,\text{disc}}$.

3.2 Part 2: sSFR sequences

In a sense, we are presenting two papers in one. However, the connections are sufficiently tight, and the data is the same, so the ideas are presented together. In what follows, we extend the sSFR-(mass ratio) diagrams in Fig. 7 to the sSFR-(stellar mass) diagrams in Fig. 8.

Using far-IR *Herschel Space Observatory* (Pilbratt et al. 2010) data and stellar mass estimates from the MAGPHYS SED-modelling program (da Cunha et al. 2008), Eales et al. (2018a) advocate for a single Galaxy Sequence to replace/unite the ‘blue sequence’ and ‘red cloud’ in the sSFR- $M_{*,\text{gal}}$ diagram. Our data support this galaxy sequence — of which the high-mass end can be seen in Fig. 8a and, for example, Wolf et al. (2009, their figure 6), — but also reveals that this is not the complete picture. The dust-poor S0 galaxies are missing from this single Galaxy Sequence. They reside in a part of the diagram where sample selection effects make them difficult to detect due to their lower stellar mass and low dust content. Their absence is not a new result; Eales et al. (2018a) note that their survey missed these low-mass ETGs. However, because they are nearby, our *WISE* data detect many of them with $-12 \lesssim sSFR_{*,\text{galaxy}} \lesssim -13$ dex, while others only have upper limits with $sSFR_{*,\text{galaxy}} \lesssim -14$ dex (Fig. 8a). While Bait et al. (2017, see their figure 10) does not identify primordial dust-poor S0 galaxies as separate from wet-merger-built dust-rich S0 galaxies, they do observe the sSFR to track the E/S0/early-type S/late-type S galaxy morphology.¹⁴

The dust-rich ETGs/S0 galaxies, which are more massive, ap-

¹⁴ A greater fraction of low-mass ($< 3 \times 10^{10} M_{\odot}$) S0 galaxies in the sample of Bait et al. (2017) would have modified their results for quenched galaxies, with S0 galaxies no longer predominantly occurring in the ‘green valley’, but their observation that the ‘green valley’ is dominated by S0 galaxies and early-type S galaxies would still hold.

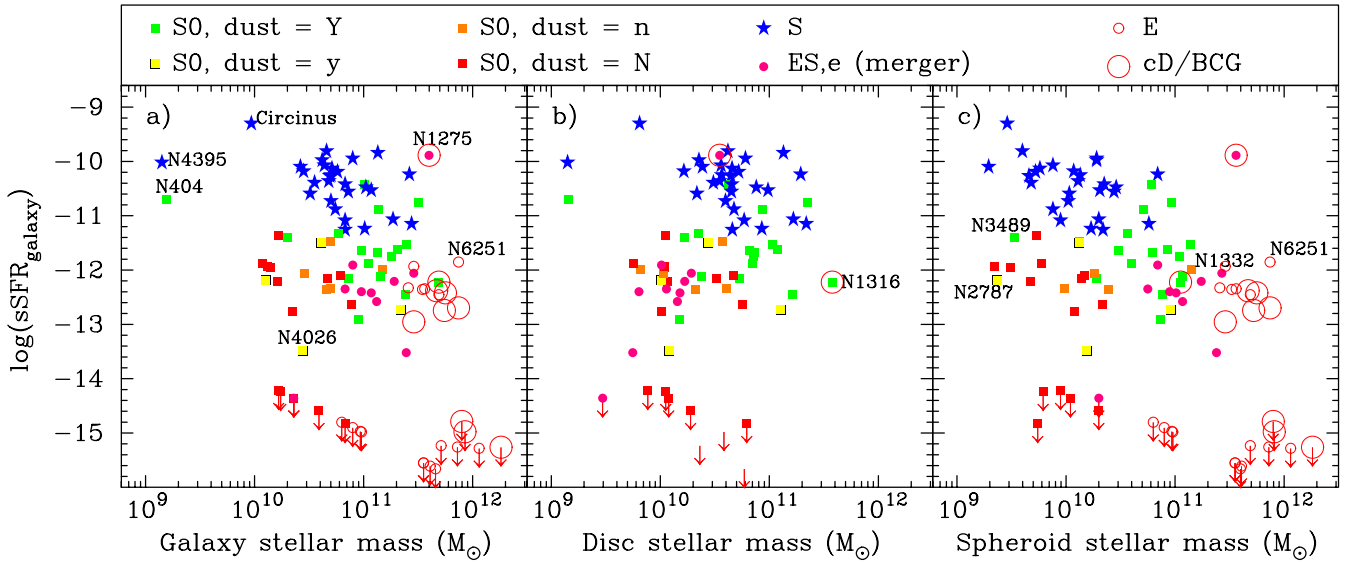


Figure 8. Left: Galaxy $s\text{SFR}_{\text{galaxy}}$ versus $M_{*,\text{galaxy}}$. The dust-poor S0 galaxies reside to the lower-left of the S-(dust-rich S0)-E SFR main sequence. As indicated by the data points that are upper limits, there is an artificial absence of systems in the lower-left of this diagram due to limitations of detection of low $s\text{SFR}$ in low-mass galaxies. Middle: Galaxy $s\text{SFR}_{\text{galaxy}}$ versus $M_{*,\text{disc}}$. While most BCGs in the sample are E galaxies, NGC 1316 is a dusty S0 galaxy, and NGC 1275 is an ES,e galaxy. Right: The bridging nature of the dust-rich S0 galaxies, between the S and E galaxies, is more apparent here when using the spheroids’ stellar mass on the horizontal axis.

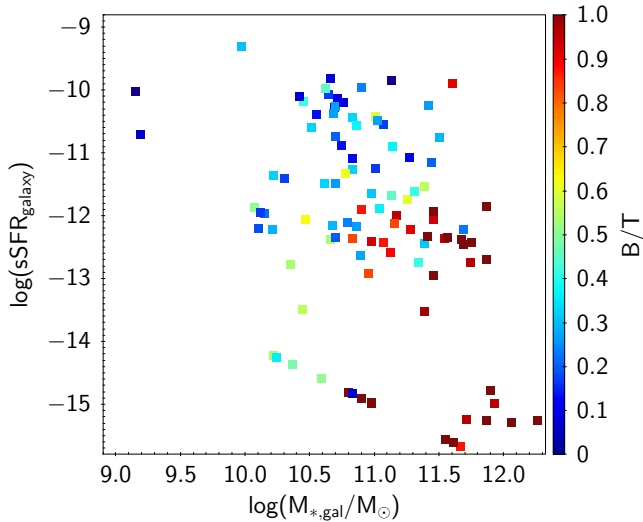


Figure 9. Similar to the left panel of Fig. 8 but showing the bulge-to-total (B/T) flux ratio rather than the morphological type. As in Fig. 8, $s\text{SFR}$ s below 10^{-14} are upper limits. In the upper right, the high B/T galaxy NGC 1275 has an artificially high $s\text{SFR}$ due to dust-heating from its AGN, as does Circinus, which has the highest $s\text{SFR}$ of the sample.

pear red in the optical colour-magnitude diagram (Graham & Sahu 2023a). This is because the dust obscures (and is heated by) the blue and UV light from the regions of younger stars (e.g. Gallazzi et al. 2009). With mid-IR observations focussing on the warm glow of the dust, we have a better estimate of the SFR than optical (wide-band) colours would provide. This has allowed the so-called ‘green valley’ (e.g., Faber et al. 2007; Schiminovich et al. 2007; Zibetti et al. 2007), usually a zone with low occupation numbers, to bloom

(Oemler et al. 2017). The mid-IR observations apparently uncover more of these transitional galaxies, with implications for our understanding of valley crossing times. The dust-rich S0 galaxies are likely the inhabitants of the ‘green mountain’ reported by Eales et al. (2018a) and Eales et al. (2018b) to form a substantial population/bridge between the S and E galaxies, yielding the single Galaxy Sequence that they report. That is, we associate the abundance of ‘green’ galaxies primarily with major wet mergers rather than, for example, fading S galaxies (Spitzer & Baade 1951; Gunn & Gott 1972; Larson et al. 1980), bulge growth via secular evolution in S galaxies (Belfiore et al. 2017), or AGN feedback (e.g. Leslie et al. 2016; Terrazas et al. 2016).

In passing, we note that while the removal of gas and fading of S galaxies will not reduce their spheroid’s stellar mass, i.e., will not shift them to the left in Fig. 5a, there are a few dust-poor S0 galaxies on the S galaxy $M_{\text{bh}}-M_{*,\text{sph}}$ relation, near the Milky Way and with intermediate $s\text{SFR}$ s (Fig. 5). These could be gas-stripped, strangled and failed S galaxies (e.g., Spitzer & Baade 1951; Arag3n-Salamanca et al. 2006; Kawata & Mulchaey 2008; Bait et al. 2017; Rathore et al. 2022), different to the bulk of the dust-poor S0 galaxies and the quenching merger products, i.e., the dust-rich S0 galaxies. It would also be of interest to know if the galaxies with centrally-located low ionisation emission line regions, found in the ‘green valley’ (Belfiore et al. 2017), might be misidentified dust-rich S0 galaxies rather than S galaxies.

Fig. 8a reveals that, on its own, the galaxies’ stellar mass is not responsible for reducing the $s\text{SFR}$, a notion explored by Peng et al. (2010). Conceivably, if this ‘mass quenching’ operated in tandem with ‘environmental quenching’, it could match the pattern seen in Fig. 8a if the dust-poor S0 galaxies reside in clusters. While the Appendix of Graham (2023b) provides the environment of the S0 galaxies used here, further detail, such as the presence/nature of a hot X-ray halo, was required for the impact of the environment to be known. However, environmental quenching addresses only half

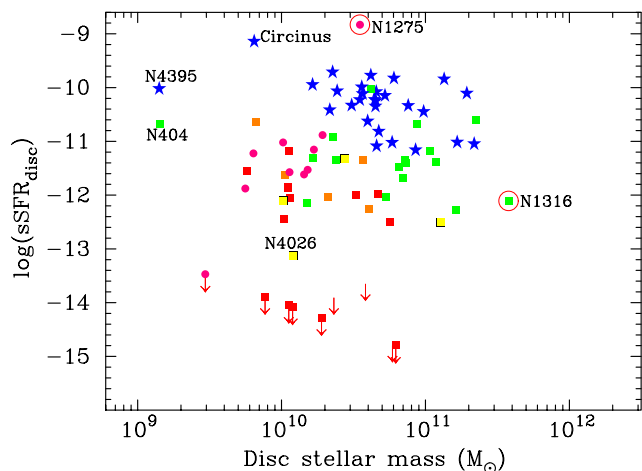


Figure 10. Similar to the middle panel of Fig. 8 but showing the *disc* $sSFR_{disc}$ versus $M_{*,disc}$.

or less of the equation. Galaxies not only evolve, or rather stagnate, through quenching, but they also grow through accretions and acquisitions. Indeed, this dictates the speciation of galaxies (Graham 2023c). It, therefore, seems likely that the galaxy morphology, a mirror to its merger history, coupled with ‘environmental quenching’, reflects the actual driving forces of galaxy evolution rather than ‘mass quenching’ coupled with ‘environment quenching’ (Peng et al. 2010). The system’s mass, which tends to correlate with the number of major mergers, would then be a secondary, consequential factor.

Eales et al. (2020) ask, Do bulges stop stars from forming? Fig. 8c plots the $sSFR$ versus the bulge stellar mass. While there is a sequence from spirals to dust-rich S0s to ES,e and E galaxies, it is also apparent that the non-dusty S0 galaxies with the same bulge masses as the S galaxies have very different $sSFR$ s. This observation is perhaps better illustrated by plotting the $sSFR$ versus the bulge-to-total stellar mass ratio (Fig. 7c). It is clear from Fig. 8c that the bulge mass does not drive the star-forming sequence. Galaxies with the same bulge mass may be a dust-poor S0 galaxy with no substantial star formation or a spiral galaxy with ample star formation.

Furthermore, spheroids with a range of stellar mass from a few billion to a trillion solar masses may be associated with galaxies having little to no star formation, evidenced by the dust-poor S0 and E galaxies. On the other hand, a trend of decreasing $sSFR$ with increasing galaxy (and spheroid) stellar mass exists for the restricted sample of S, dust-rich S0, and E galaxies. However, as noted, this ignores many intermediate-to-low mass galaxies, which dominate the galaxy mass function by number, are disc-dominated, and predominantly dust-poor.

Fig. 9 is a variant of Fig. 8a. It shows the B/T flux ratios rather than the morphological types. In so doing, it provides an alternative view for the result seen in Fig. 7c. Specifically, it shows that the B/T ratio does not dictate the $sSFR$ of galaxies. The morphology of the galaxies — which better reflects their formation history — appears to be a more apt tracer of the $sSFR$ (Fig. 8a). Most large surveys have a relatively coarse estimate of galaxy morphology, which often results in a rather large bag of uncertain or intermediate galaxy types. As such, they tend to miss what is revealed here by using a sample with precise morphologies. Other compli-

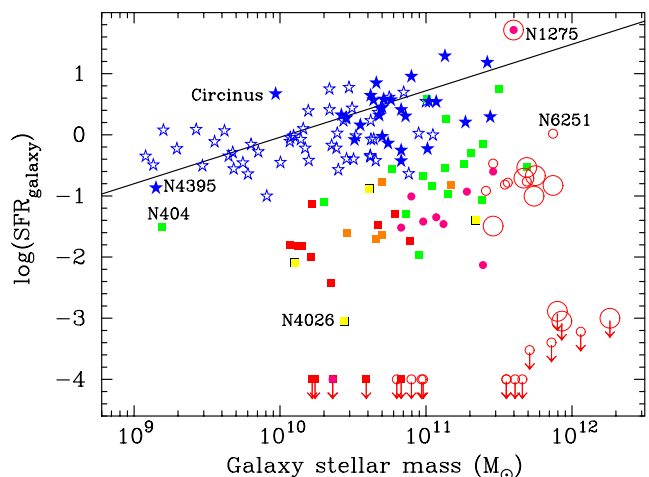


Figure 11. SFR versus galaxy stellar mass. The black line is the star-forming main sequence from Renzini & Peng (2015), without any adjustment for potentially different galaxy luminosities and stellar mass-to-light ratios between studies. The dust-rich S0 galaxies, shown in green, are the population which form the high-mass bridge (aka ‘green mountain’: Eales et al. 2018b) between the blue star-forming sequence and the red cloud. The Virgo Cluster spiral galaxies from Soria et al. (2022) have been included (open stars). As noted in the text, SFR detection limits make it challenging to populate the lower-left of the diagram with the low-mass ETGs that dominate the Universe by number and which are included in the van den Bergh (1976) Trident, the ATLAS^{3D} Comb (Cappellari et al. 2011), and the Triangal (Graham 2023c). This will be pursued in future work.

cations with large surveys can arise from the necessarily automated bulge/disc decompositions of thousands of galaxies. For example, many S0 and S galaxies contain substantial bars, and the combined flux from the bulge+bar can result in a Sérsic model bulge with an overly large Sérsic index, size, and flux for what is supposed to be just the bulge. In addition, many discs do not have a simple exponential profile, but require a truncated, anti-truncated, or inclined disc model (not typically used by the automated routines) in order to obtain the correct B/T ratio. Bypassing decompositions, the radial concentration of stars in a galaxy, which varies monotonically with the galaxy’s Sérsic index (Trujillo et al. 2001), is sometimes used as a tracer of galaxy type. In practice, this, too can be problematic for a couple of reasons. Measures of concentration using radii thought to contain 80-90 per cent of the total galaxy flux can be highly sensitive to the image exposure depth when the Sérsic index is high (Graham et al. 2001). This can hinder the separation of pure E galaxies from S0 galaxies with big bulges. Second, even when measured correctly, LTGs and low-mass ETGs can have the same low measure of concentration. Therefore, the concentration is not always a good discriminant for separating ETGs from LTGs.

In the current sample, the S and the dust-rich S0 galaxies have a similar range of stellar-disc masses, while the S galaxies have the higher $sSFR$ s (Fig. 8b). Readers are reminded that the $sSFR$ is typically the SFR divided by the *galaxy*, rather than the *disc*, stellar mass. Suppose the bulk of new star formation occurs in galactic discs, where gas can condense and cool. In that case, it may make more sense to consider trends involving the star formation rate plotted against the stellar-disc mass or, equally, the *discs’* specific SFR versus the *discs’* stellar mass. In Fig. 10, we use $sSFR_{disc}$, the SFR normalised by the stellar-disc mass. Due to the dominance of the disc’s stellar mass in most disc galaxies, the trend is

qualitatively similar to that seen in the $\text{sSFR}_{\text{galaxy}}-M_{*,\text{disc}}$ diagram (Fig. 8b). However, as can be sensed from the distribution of bulge-to-total stellar mass ratios in Fig. 7c, this slightly elevates the sSFR for some S0 galaxies and considerably so for the ES,e galaxies with their intermediate-scale discs. Using $\text{sSFR}_{\text{disc}}$ rather than $\text{sSFR}_{\text{galaxy}}$ reduces the gap seen in Fig. 8b.

We next close the loop by returning to the $\text{SFR}_{\text{galaxy}}-M_{*,\text{galaxy}}$ diagram (Fig. 3) with our full sample now shown in Fig. 11 using the *Spitzer*-based stellar masses (Section 2.2). This compares well with Lutz et al. (2021, their figure 1). The black line in Fig. 11 shows the relation from Renzini & Peng (2015) for the star-forming main sequence. Fig. 11 also includes the LTGs from Soria et al. (2022), better revealing the extent of the star-forming main sequence than the sample with directly measured BH masses. For these Virgo LTGs, the SFR rate has been calculated using *WISE* photometry and the process described in Section 2.3. The stellar masses are derived consistently with that used to obtain the *Spitzer*-based stellar masses for the sample with directly measured BH masses. For this additional LTG sample, this was done using the $3.6\ \mu\text{m}$ (AB) galaxy apparent magnitudes from the *Spitzer* Survey of Stellar Structure in Galaxies (S⁴G: Sheth et al. 2010) catalog¹⁵. The distances from Soria et al. (2022, their table 1, column 8) and the following $(B - V)$ -dependent (stellar mass)-to-light ratio from Graham & Sahu (2023a, their equation 4) was also used

$$\log(M_*/L_{3.6}) = 1.034(B - V) - 1.067. \quad (2)$$

In total, 56 LTGs with both B and V magnitudes were included.

Fig. 11 also displays the steep decline in star-formation rate as one progresses from massive ($\gtrsim \text{few } 10^{10} M_{\odot}$) spiral galaxies to more massive, dust-rich S0 galaxies and then to E galaxies and BCGs, which are predominantly E galaxies. This connection led Eales et al. (2018b) to advocate for a single sequence connecting the spiral galaxies with the E galaxies. A more complete picture connecting the galaxies involves the triangular-shaped evolutionary sequence created by Graham (2023c) and referred to there as the ‘Triangal’. For the first time, in the following section, this merger-induced pattern of galaxy growth and metamorphism is revealed through the $\text{sSFR}-M_*$ diagram (Fig. 12).

3.2.1 The Schema

Here we provide an interpretation of the patterns seen in the $\text{sSFR}-M_*$ diagram.

As revealed through Fig. 5a and discussed in Graham (2023c), the growth of classical bulges and SMBHs commences with low-mass and dust-poor S0 galaxies. If low-mass galaxies enter the hot X-ray-emitting gas halo of a large galaxy group or cluster, their reservoir of high-angular momentum cold gas (e.g., Carignan & Beaulieu 1989; Pildis et al. 1997; van Zee et al. 1997; Deg et al. 2023) will be ram-pressure stripped, along with any dust clouds (Gunn & Gott 1972; Yagi et al. 2010; Merluzzi et al. 2013). These galaxies may not have experienced a significant accretion event, gravitational perturbation, or disc-instability that would lead them to blossom into an S galaxy. Due to their cluster-stunting growth, they may be primordial galaxies, albeit with an evolved/aged stellar population (Rakos & Schombert 2004; Marcum et al. 2004; Paudel et al. 2010; Sii’chenko 2013). Typically having small B/T ratios (Graham 2023c, figure A2), and thus held-up by rotation, they are

¹⁵ <http://cdsarc.unistra.fr/viz-bin/nph-Cat/html?J/PASP/122/1397/s4g.dat.gz>

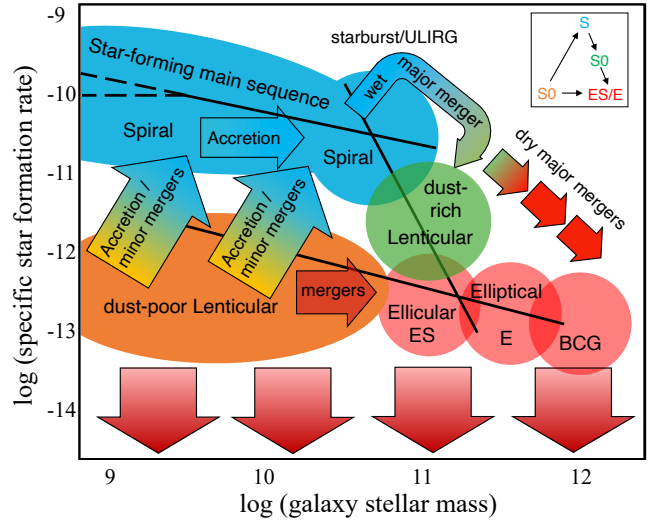


Figure 12. Stellar-mass growth sequence from Graham (2023c), tracking the morphological evolution of galaxies. (Graham & Sahu 2023b, presents non-growth pathways involving the rapid cessation of star formation or the removal of stars.) The upper line is the ‘star-forming main sequence’, while the lower line demarcates the upper envelope of the dust-poor ETGs. The steep line on the right tracks the bright galaxy sequence (e.g., Eales et al. 2018a, their figure 3) as star formation fades after fuel-consuming merger events and dry mergers. The schema shown here captures the left-hand panel of Fig. 8, with insight from Fig. 3. Tidal disturbances can send high-(angular momentum) gas inward, and dwarf/satellite galaxy accretion can induce spiral arms, thereby, primarily in the younger Universe, elevating galaxies that were once equivalent to the progenitors of today’s dust-poor S0 galaxies onto the star-forming main sequence. Most of these S0-to-S transitions likely occurred in the past, while (major merger)-induced S-to-S0 transitions are expected to occur in the past, present, and future. After the potential starbursts from these gas-rich S galaxy collisions fade, it produces the dust-rich S0 galaxies in/near the ‘green valley’ of the colour-mass diagram. Merging of these dust-rich S0 galaxies produces the E galaxies. Selection biases are such that the low-mass dust-poor S0 galaxies with low sSFRs are preferentially missed by surveys seeking star-forming galaxies (as noted by Eales et al. 2018a, their figure 3). This can partly be rectified with a V/V_{max} correction (e.g., Renzini & Peng 2015, their figure 4).

ETGs. On the other hand, if they are still in the field or a small group environment, they may retain substantial HI fuel reserves, waiting for the right gravitational disturbance (or capture/merger) to zap the angular momentum of these gas reserves and send it inward. This can reinvigorate star formation (Li et al. 2008) and induce a spiral wave (e.g., Kumar et al. 2022), as can captured (and internal) gravitational perturbers (D’Onghia et al. 2013), taking systems onto the spiral galaxy sequence. This should not be a surprising origin for the S galaxies; in simulations and theories to explain the creation of S galaxies, one commences with a spiral-less disc galaxy, an S0 galaxy. The S galaxies can be built-up from (S0 galaxies via) minor mergers (Brook et al. 2004), satellite capture (Law et al. 2005; Martínez-Delgado et al. 2010), and gas accretion via cold flows from either the cosmic web, disturbed high-angular-momentum gas clouds, or a cooling hot-gas halo (Dekel & Birnboim 2006; Brooks et al. 2009; Moster et al. 2011; Lutz et al. 2017). This increases their SFR, and recycling material from the new stellar winds produces a rolling tail of star formation (in-situ) until the next accretion/merger fuelled burst.

Mergers also bring in new stars (ex-situ) and can redistribute

pre-existing disc stars into the bulge component of a galaxy. Quantifying this latter development, coupled with the morphological transition of galaxy type, i.e., the speciation of galaxies (Graham 2023c), could help further advance some galaxy mass growth models (e.g. Moster et al. 2013; Mutch et al. 2013). Rather than treating galaxies as structureless entities with a single stellar mass — as done in many surveys and cosmological and semi-analytical simulations — a galaxy component analysis (e.g., Allen et al. 2006; Krajnović et al. 2013; Casura et al. 2022) and morphological awareness¹⁶ should aid a fuller understanding of the mass assembly of galaxies (Bundy et al. 2006; Kauffmann et al. 2006; Pérez-González et al. 2008; Ilbert et al. 2013; Driver et al. 2022) and the size evolution of discs, bulges and galaxies (Daddi et al. 2005; Trujillo et al. 2006; van der Wel et al. 2014). Indeed, the benchmark $z \sim 0$ size-mass relation for bulges is quite different to that of galaxies (e.g., Hon et al. 2023, and references therein).

The broad bend in the star-forming main sequence around $\sim 10^9 M_{\odot}$ was explored by Popesso et al. (2019) at $z \sim 0$ and Whitaker et al. (2014) over a range of redshifts from 0.5 to 2.5. Although not strong, a bend appears evident in the ($z \sim 0$) S⁴G data (Fig. 3). This might be partly due to the presence of low-mass S0→S transition objects. The detection and inclusion of such galaxies reduce the sample’s median SFR at a fixed stellar mass, shifting the median below the star-forming main sequence ‘ridge line’ detected by Renzini & Peng (2015) and shown in Fig. 11.

Rathore et al. (2022) have suggested that minor mergers are a driving influence in rejuvenating star formation in S0 galaxies. Major mergers can also do this. Major wet mergers of S galaxies can induce a starburst (Solomon et al. 1997), build up the bulge using pre-existing disc stars (Naab & Burkert 2003; Bois et al. 2011), and possibly (in the past when more gas was available) yield an ultraluminous infrared galaxy (ULIRG; Sanders et al. 1988) whose SFR will decay according to some gas consumption timescale, modulo no further significant accretion of gas. The associated enhancement in dust, evident in the prototypical starburst galaxy M82 (Yoshida et al. 2019), likely arises from the condensation of metals as the metal-enriched gas cools to form a new generation of stars (Origlia et al. 2004; Sharda et al. 2021). As such, the dust-to-gas ratio may be elevated in dust-rich S0 galaxies, and their gas-to-stellar mass ratio is reduced in the evolved dust-rich S0 galaxies. That is, the notion of a near-constant dust-to-gas ratio is not expected to apply across the spectrum of disc-dominated galaxies. Indeed, the dust-to-HI gas ratio increases with metallicity, [O/H], (Engelbracht et al. 2008, their figure 6). This dust and metal build-up in galaxies with increasing stellar mass (e.g., Charlot et al. 2002; Jiménez et al. 2011) works in tandem with galactic winds and ram-pressure stripping, which operate more effectively at lower masses (e.g. Tremonti et al. 2004; Mayer et al. 2006).

A major merger of two dust-rich S0 galaxies erodes the stellar discs. It yields a massive elliptical galaxy or an ES galaxy if some remnant disc remains. Decades ago, it was speculated that colliding S galaxies would generate a hot mess, i.e., an elliptical galaxy (Toomre 1977). However, subsequent modellers pointed out that unless there are specially contrived orbital encounters, it typically

takes more than one major merger for the net rotation, and thus discs, to entirely cancel (e.g., Barnes & Hernquist 1996; Naab & Burkert 2003). A major collision of sufficiently massive dust-poor S0 galaxies may bypass the S galaxy phase to create an S0 with a more massive spheroid. The dusty nature of the massive S0 galaxies suggests their creation involved wet rather than dry mergers, perhaps occurring in a much younger Universe (when today’s dust-poor S0 galaxies were gas-rich).

The chain of events noted above is shown in Fig. 12. The schematic seen there is a direct mapping of the quasi-triangular-shaped galaxy anatomy sequence, with evolutionary pathways, introduced in Graham (2023c). Although not explored here, one would expect clumpiness and asymmetry to broadly track the morphological types shown in Fig. 12, from smooth and symmetric (dust-poor S0 galaxies) to the opposite appearance (S galaxies, starbursts) to a middle ground (dust-rich S0 and some ES galaxies) before settling back down to a more smooth and relaxed appearance (E galaxies). As suggested in Graham (2023c), the lower-limit to the dust-poor S0 galaxies may extend into the realm of the low central surface brightness ETGs Sandage & Binggeli (1984), nowadays referred to as ultra diffuse galaxies (aka UDGs van Dokkum et al. 2015).

4 SUMMARY

Armed with the (galaxy morphology)-dependent $M_{\text{bh}}-M_{*,\text{sph}}$ sequences (Fig. 5a), other trends in this diagram can be better understood, such as the distribution of star formation rates (Fig. 5b). For instance, after identifying the spiral and dust-rich lenticular galaxies, it is apparent they are bookended by low-star-formation (dust-poor S0 and E) galaxies. Without substantial numbers of low-mass S0 galaxies, and excluding mergers like NGC 5128 (Cen A), something of an over-arching band (rather than bookends) of low-SFR galaxies appears above the S galaxies in this diagram (Savorgnan et al. 2016; Terrazas et al. 2017). That is, with a restricted sample, quiescent galaxies appear to have more massive black holes than star-forming galaxies at a given stellar mass, suggesting a role for AGN feedback, with higher M_{bh}/M_* ratios quenching star formation.

However, this is an incomplete picture. Fig. 7 reveals that the galaxy morphology is a better indicator of the sSFR than the M_{bh}/M_* ratio. It is also a better indicator than the prominence of the bulge, quantified by the $M_{*,\text{sph}}/M_{*,\text{gal}}$ ratio. We additionally show that the bulge mass does not determine the occurrence on/off the star-forming main sequence. Galaxies with higher SFRs primarily have these because of refuelling events which have dictated their morphology. They are foremost spiral galaxies, or dust-rich S0 galaxies built via major wet mergers, rather than systems with a low specific black hole mass, i.e., a lower M_{bh}/M_* ratio that is less capable of quenching star formation.

Some dust-rich S0 galaxies fill the ‘green valley’, forming a bridge or ‘green mountain’ (Eales et al. 2018b) between the blue star-forming main sequence and the ‘red cloud’ of E galaxies in the (s)SFR- $M_{*,\text{gal}}$ diagram (Fig. 3 and 8). This is not due to AGN (Fig. 4) and is also evident when using the stellar mass of the disc (Fig. 10), where the bulk of the star formation occurs. The ‘red cloud’ in the (s)SFR- $M_{*,\text{gal}}$ diagram is seen to become a more extended ‘red sequence’ (or more correctly, an upper envelope) upon the inclusion of dust-poor S0 galaxies.

Fig. 12 provides a schematic representation of evolutionary pathways through the sSFR_{galaxy}- $M_{*,\text{galaxy}}$. It is an adaption of the

¹⁶ One area of mismatch that should be noted to avoid confusion is that simulators may refer to S0 galaxies, particularly the lower-mass S0 galaxies, as LTGs rather than ETGs due to their use of rotation curves and bulge-to-total stellar mass ratios for the identification of galaxy type (e.g., Vogelsberger et al. 2014), as opposed to observers who use the presence/absence of spiral structure. This differentiation is increasingly relevant at masses less than that of the Milky Way.

morphological transitions seen in Fig. 5 and previously captured by the ‘Triangal’ for understanding the speciation of galaxies (Graham 2023c).

ACKNOWLEDGEMENTS

T.H.J. is grateful for an extended visit to Swinburne University of Technology and acknowledges support from the South African National Research Foundation. This publication uses data products from the Wide-field Infrared Survey Explorer, a joint project of the University of California, Los Angeles, and the Jet Propulsion Laboratory/California Institute of Technology, funded by the National Aeronautics and Space Administration (NASA). This research has also made use of NASA’s Astrophysics Data System Bibliographic Services and the NASA/IPAC Extragalactic Database (NED), which is funded by NASA and operated by the California Institute of Technology.

5 DATA AVAILABILITY

Black hole masses, along with *SST*-derived spheroid and galaxy stellar masses, are tabulated in Graham & Sahu (2023a). The spheroid’s stellar masses are obtained from published multicomponent decompositions, which separate bars and inner discs from the spheroids (Savorgnan & Graham 2016a; Davis et al. 2019; Sahu et al. 2019; Graham & Sahu 2023b). Galaxy morphologies — including whether the E galaxies are BCG or cD, and the ‘dust bin’ of each S0 galaxy — are provided in Graham & Sahu (2023a) and Graham & Sahu (2023b), and (Graham 2023b), respectively.

REFERENCES

Allen P. D., Driver S. P., Graham A. W., Cameron E., Liske J., de Propris R., 2006, *MNRAS*, 371, 2

Aragón-Salamanca A., Bedregal A. G., Merrifield M. R., 2006, *A&A*, 458, 101

Arzoumanian Z., et al., 2020, *ApJ*, 905, L34

Athanassoula E., 2005, *MNRAS*, 358, 1477

Auclair P., et al., 2022, *arXiv e-prints*, p. arXiv:2204.05434

Bait O., Barway S., Wadadekar Y., 2017, *MNRAS*, 471, 2687

Barnes J. E., Hernquist L., 1996, *ApJ*, 471, 115

Begelman M. C., Blandford R. D., Rees M. J., 1980, *Nature*, 287, 307

Bekki K., Couch W. J., Drinkwater M. J., Gregg M. D., 2001, *ApJ*, 557, L39

Belfiore F., et al., 2017, *MNRAS*, 466, 2570

Benson A. J., Bower R. G., Frenk C. S., Lacey C. G., Baugh C. M., Cole S., 2003, *ApJ*, 599, 38

Bernardi M., Shankar F., Hyde J. B., Mei S., Marulli F., Sheth R. K., 2010, *MNRAS*, 404, 2087

Binette L., 1985, *A&A*, 143, 334

Blom C., Forbes D. A., Foster C., Romanowsky A. J., Brodie J. P., 2014, *MNRAS*, 439, 2420

Bois M., et al., 2011, *MNRAS*, 416, 1654

Bridle A. H., Perley R. A., 1984, *ARA&A*, 22, 319

Brook C. B., Kawata D., Gibson B. K., Freeman K. C., 2004, *ApJ*, 612, 894

Brooks A. M., Governato F., Quinn T., Brook C. B., Wadsley J., 2009, *ApJ*, 694, 396

Bundy K., et al., 2006, *ApJ*, 651, 120

Bunker A. J., Stanway E. R., Ellis R. S., McMahon R. G., 2004, *MNRAS*, 355, 374

Burbidge E. M., Burbidge G. R., 1965, *ApJ*, 142, 1351

Buta R., Laurikainen E., Salo H., Block D. L., Knapen J. H., 2006, *AJ*, 132, 1859

Calzetti D., 2013, in Falcón-Barroso J., Knapen J. H., eds., *Secular Evolution of Galaxies*. Cambridge University Press, Cambridge, UK, p. 419, doi:10.48550/arXiv.1208.2997

Capetti A., Marconi A., Macchetto D., Axon D., 2005, *A&A*, 431, 465

Cappellari M., et al., 2011, *MNRAS*, 416, 1680

Carignan C., Beaulieu S., 1989, *ApJ*, 347, 760

Carter D., 1978, *MNRAS*, 182, 797

Casura S., et al., 2022, *MNRAS*, 516, 942

Chabrier G., 2003, *PASP*, 115, 763

Charlot S., Kauffmann G., Longhetti M., Tresse L., White S. D. M., Maddox S. J., Fall S. M., 2002, *MNRAS*, 330, 876

Chieffi A., Limongi M., 2004, *ApJ*, 608, 405

Ciambur B. C., 2015, *ApJ*, 810, 120

Ciambur B. C., Graham A. W., 2016, *MNRAS*, 459, 1276

Cluver M. E., Jarrett T. H., Dale D. A., Smith J. D. T., August T., Brown M. J. I., 2017, *ApJ*, 850, 68

Combes F., Sanders R. H., 1981, *A&A*, 96, 164

Crane P., Vernet J., 1997, *ApJ*, 486, L91

Curti M., et al., 2023, *arXiv e-prints*, p. arXiv:2304.08516

D’Onghia E., Vogelsberger M., Hernquist L., 2013, *ApJ*, 766, 34

D’Onofrio M., Zaggia S. R., Longo G., Caon N., Capaccioni M., 1995, *A&A*, 296, 319

Daddi E., et al., 2005, *ApJ*, 626, 680

Davis B. L., Graham A. W., Seigar M. S., 2017, *MNRAS*, 471, 2187

Davis B. L., Graham A. W., Cameron E., 2018, *ApJ*, 869, 113

Davis B. L., Graham A. W., Cameron E., 2019, *ApJ*, 873, 85

Deg N., et al., 2023, *arXiv e-prints*, 525, 4663–4684

Dekel A., Birnboim Y., 2006, *MNRAS*, 368, 2

Draine B. T., Salpeter E. E., 1979, *ApJ*, 231, 438

Driver S. P., et al., 2022, *MNRAS*, 513, 439

Eales S., et al., 2018a, *MNRAS*, 473, 3507

Eales S. A., et al., 2018b, *MNRAS*, 481, 1183

Eales S., Eales O., de Vis P., 2020, *MNRAS*, 491, 69

Engelbracht C. W., Rieke G. H., Gordon K. D., Smith J. D. T., Werner M. W., Moustakas J., Willmer C. N. A., Vanzì L., 2008, *ApJ*, 678, 804

Erwin P., Beltrán J. C. V., Graham A. W., Beckman J. E., 2003, *ApJ*, 597, 929

Faber S. M., et al., 2007, *ApJ*, 665, 265

Fazio G. G., et al., 2004, *ApJS*, 154, 10

Fedorova E., Vasylenko A., Hnatyk B. I., Zhdanov V. I., 2016, *Astronomische Nachrichten*, 337, 96

Filippenko A. V., Sargent W. L. W., 1985, *ApJS*, 57, 503

Fort B. P., Prieur J. L., Carter D., Meatheringham S. J., Vigroux L., 1986, *ApJ*, 306, 110

Gail H. P., Sedlmayr E., 1988, *A&A*, 206, 153

Gallazzi A., et al., 2009, *ApJ*, 690, 1883

Galliano F., et al., 2021, *A&A*, 649, A18

Goncalves A. C., Veron P., Veron-Cetty M. P., 1998, *A&A*, 333, 877

Goudfrooij P., Gilmore D., Whitmore B. C., Schweizer F., 2004, *ApJ*, 613, L121

Graham A. W., 2004, *ApJ*, 613, L33

Graham A. W., 2012, *ApJ*, 746, 113

Graham A. W., 2019, *MNRAS*, 487, 4995

Graham A. W., 2023a, *MNRAS*, 518, 6293

Graham A. W., 2023b, *MNRAS*, 521, 1023

Graham A. W., 2023c, *MNRAS*, 522, 3588

Graham A. W., Driver S. P., 2005, *Publ. Astron. Soc. Australia*, 22, 118

Graham A. W., Sahu N., 2023a, *MNRAS*, 518, 2177

Graham A. W., Sahu N., 2023b, *MNRAS*, 520, 1975

Graham A. W., Scott N., 2013, *ApJ*, 764, 151

Graham A. W., Scott N., 2015, *ApJ*, 798, 54

Graham A. W., Trujillo I., Caon N., 2001, *AJ*, 122, 1707

Graham A. W., Jerjen H., Guzmán R., 2003, *AJ*, 126, 1787

Graham A. W., Soria R., Davis B. L., 2019, *MNRAS*, 484, 814

Graham A. W., Soria R., Ciambur B. C., Davis B. L., Swartz D. A., 2021, *ApJ*, 923, 146

- Gunn J. E., Gott J. Richard I., 1972, *ApJ*, 176, 1
- Hernquist L., Spergel D. N., 1992, *ApJ*, 399, L117
- Ho L. C., Filippenko A. V., Sargent W. L. W., Peng C. Y., 1997, *ApJS*, 112, 391
- Hohl F., 1975, in Hayli A., ed., *International Astronomical Union Symposia Vol. 69, Dynamics of Stellar Systems*. Dordrecht; Boston: D. Reidel Pub. Co., p. 349
- Hon D. S. H., Graham A. W., Sahu N., 2023, *MNRAS*, 519, 4651
- Hopkins P. F., Hernquist L., Cox T. J., Kereš D., 2008, *ApJS*, 175, 356
- Hubble E. P., 1926, *ApJ*, 64, 321
- Hubble E. P., 1936, *Realm of the Nebulae*. New Haven: Yale University Press
- Huchra J. P., Wyatt W. F., Davis M., 1982, *AJ*, 87, 1628
- Ilbert O., et al., 2013, *A&A*, 556, A55
- Into T., Portinari L., 2013, *MNRAS*, 430, 2715
- Irwin J. A., Stil J. M., Bridges T. J., 2001, *MNRAS*, 328, 359
- Israel F. P., 1998, *A&ARv*, 8, 237
- Jarrett T. H., et al., 2011, *ApJ*, 735, 112
- Jarrett T. H., Cluver M. E., Brown M. J. I., Dale D. A., Tsai C. W., Masci F., 2019, *ApJS*, 245, 25
- Jarrett T. H., Cluver M. E., Taylor E. N., Bellstedt S., Robotham A. S. G., Yao H. F. M., 2023, *ApJ*, 946, 95
- Jarvis B. J., 1986, *AJ*, 91, 65
- Jeans J. H., 1919, *Problems of cosmogony and stellar dynamics*. Cambridge Univ. Press, Cambridge
- Jedrzejewski R. I., 1987, *MNRAS*, 226, 747
- Jerjen H., Kalnajs A., Binggeli B., 2000, *A&A*, 358, 845
- Jiménez N., Cora S. A., Bassino L. P., Tecce T. E., Smith Castelli A. V., 2011, *MNRAS*, 417, 785
- Kailey W. F., Lebofsky M. J., 1988, *ApJ*, 326, 653
- Kauffmann G., Heckman T. M., De Lucia G., Brinchmann J., Charlot S., Tremonti C., White S. D. M., Brinkmann J., 2006, *MNRAS*, 367, 1394
- Kawata D., Mulchaey J. S., 2008, *ApJ*, 672, L103
- Keel W. C., et al., 2015, *AJ*, 149, 155
- Kim M., et al., 2015, *ApJ*, 814, 8
- Kirkpatrick A., Pope A., Sajina A., Roebuck E., Yan L., Armus L., Díaz-Santos T., Stierwalt S., 2015, *ApJ*, 814, 9
- Kormendy J., Richstone D., 1995, *ARA&A*, 33, 581
- Krajnović D., et al., 2013, *MNRAS*, 432, 1768
- Kroupa P., 2002, *Science*, 295, 82
- Kumar A., Ghosh S., Kataria S. K., Das M., Debattista V. P., 2022, *MNRAS*, 516, 1114
- Laor A., 2001, *ApJ*, 553, 677
- Larson R. B., Tinsley B. M., Caldwell C. N., 1980, *ApJ*, 237, 692
- Lauer T. R., 1988, *ApJ*, 325, 49
- Law D. R., Johnston K. V., Majewski S. R., 2005, *ApJ*, 619, 807
- Leslie S. K., Kewley L. J., Sanders D. B., Lee N., 2016, *MNRAS*, 455, L82
- Li C., Kauffmann G., Heckman T. M., Jing Y. P., White S. D. M., 2008, *MNRAS*, 385, 1903
- Liller M. H., 1966, *ApJ*, 146, 28
- Limongi M., Chieffi A., 2003, *ApJ*, 592, 404
- Liu F. K., Xie G. Z., 1992, *A&AS*, 95, 249
- Liu F. K., Zhang Y. H., 2002, *A&A*, 381, C7
- Lundmark K., 1925, *MNRAS*, 85, 865
- Lundmark K., 1927, *Nova Acta Regiae Soc. Sci. Upsaliensis Ser. V*, pp 1–127
- Lutz K. A., et al., 2017, *MNRAS*, 467, 1083
- Lutz K. A., et al., 2021, *A&A*, 649, A39
- Magorrian J., et al., 1998, *AJ*, 115, 2285
- Maia M. A. G., Machado R. S., Willmer C. N. A., 2003, *AJ*, 126, 1750
- Maraston C., Pforr J., Renzini A., Daddi E., Dickinson M., Cimatti A., Tonini C., 2010, *MNRAS*, 407, 830
- Marcum P. M., Aars C. E., Fanelli M. N., 2004, *AJ*, 127, 3213
- Martig M., Bournaud F., 2010, *ApJ*, 714, L275
- Martig M., Bournaud F., Teyssier R., Dekel A., 2009, *ApJ*, 707, 250
- Martínez-Delgado D., et al., 2010, *AJ*, 140, 962
- Matsuura M., et al., 2011, *Science*, 333, 1258
- Mayer L., Mastroiello C., Wadsley J., Stadel J., Moore B., 2006, *MNRAS*, 369, 1021
- Merluzzi P., et al., 2013, *MNRAS*, 429, 1747
- Middleton H., Sesana A., Chen S., Vecchio A., Del Pozzo W., Rosado P. A., 2021, *MNRAS*, 502, L99
- Mihos J. C., Richstone D. O., Bothun G. D., 1992, *ApJ*, 400, 153
- Milosavljević M., Merritt D., 2001, *ApJ*, 563, 34
- Mirabel I. F., et al., 1999, *A&A*, 341, 667
- Moore B., Katz N., Lake G., Dressler A., Oemler A., 1996, *Nature*, 379, 613
- Moster B. P., Macciò A. V., Somerville R. S., Naab T., Cox T. J., 2011, *MNRAS*, 415, 3750
- Moster B. P., Naab T., White S. D. M., 2013, *MNRAS*, 428, 3121
- Mutch S. J., Croton D. J., Poole G. B., 2013, *MNRAS*, 435, 2445
- Naab T., Burkert A., 2003, *ApJ*, 597, 893
- Oemler Augustus J., Abramson L. E., Gladders M. D., Dressler A., Poggianti B. M., Vulcani B., 2017, *ApJ*, 844, 45
- Origlia L., Ranalli P., Comastri A., Maiolino R., 2004, *ApJ*, 606, 862
- Panessa F., Bassani L., 2002, *A&A*, 394, 435
- Patterson F. S., 1940, *Harvard College Observatory Bulletin*, 914, 9
- Paudel S., Lisker T., Kuntschner H., Grebel E. K., Glatt K., 2010, *MNRAS*, 405, 800
- Peng Y.-j., et al., 2010, *ApJ*, 721, 193
- Pérez-González P. G., et al., 2008, *ApJ*, 675, 234
- Perley R. A., Bridle A. H., Willis A. G., 1984, *ApJS*, 54, 291
- Pilbratt G. L., et al., 2010, *A&A*, 518, L1
- Pildis R. A., Schombert J. M., Eder A., 1997, *ApJ*, 481, 157
- Popesso P., et al., 2019, *MNRAS*, 483, 3213
- Popesso P., et al., 2023, *MNRAS*, 519, 1526
- Rakos K., Schombert J., 2004, *AJ*, 127, 1502
- Rathore H., Kumar K., Mishra P. K., Wadadekar Y., Bait O., 2022, *MNRAS*, 513, 389
- Renzini A., Peng Y.-j., 2015, *ApJ*, 801, L29
- Reynolds J. H., 1920, *MNRAS*, 80, 746
- Reynolds J. H., 1925, *MNRAS*, 85, 1014
- Robertson B. E., et al., 2023, *Nature Astronomy*, 7, 611
- Roediger J. C., Courteau S., 2015, *MNRAS*, 452, 3209
- Saha K., Graham A. W., Rodríguez-Herranz I., 2018, *ApJ*, 852, 133
- Sahu N., Graham A. W., Davis B. L., 2019, *ApJ*, 876, 155
- Sahu N., Graham A. W., Davis B. L., 2020, *ApJ*, 903, 97
- Sahu N., Graham A. W., Hon D. S. H., 2023, *MNRAS*, 518, 1352
- Salim S., Boquien M., Lee J. C., 2018, *ApJ*, 859, 11
- Salucci P., Ratnam C., Monaco P., Danese L., 2000, *MNRAS*, 317, 488
- Sandage A., Binggeli B., 1984, *AJ*, 89, 919
- Sanders D. B., Soifer B. T., Elias J. H., Madore B. F., Matthews K., Neugebauer G., Scoville N. Z., 1988, *ApJ*, 325, 74
- Savorgnan G. A. D., Graham A. W., 2016a, *ApJS*, 222, 10
- Savorgnan G. A. D., Graham A. W., 2016b, *MNRAS*, 457, 320
- Savorgnan G. A. D., Graham A. W., Marconi A., Sani E., 2016, *ApJ*, 817, 21
- Schiminovich D., et al., 2007, *ApJS*, 173, 315
- Scott N., Graham A. W., Schombert J., 2013, *ApJ*, 768, 76
- Scoville N. Z., et al., 2000, *AJ*, 119, 991
- Searle L., 1965, *Nature*, 207, 1282
- Sérsic J. L., 1963, *Boletín de la Asociación Argentina de Astronomía La Plata Argentina*, 6, 41
- Shankar F., et al., 2016, *MNRAS*, 460, 3119
- Sharda P., Krumholz M. R., Wisnioski E., Acharyya A., Federrath C., Forbes J. C., 2021, *MNRAS*, 504, 53
- Sheth K., et al., 2010, *PASP*, 122, 1397
- Sil'chenko O., 2013, *Memorie della Società Astronomica Italiana Supplementi*, 25, 93
- Sil'chenko O. K., Afanasiev V. L., 2004, *AJ*, 127, 2641
- Solomon P. M., Downes D., Radford S. J. E., Barrett J. W., 1997, *ApJ*, 478, 144
- Soria R., et al., 2022, *MNRAS*, 512, 3284
- Spitzer L., Baade W., 1951, *ApJ*, 113, 413

- Stalevski M., González-Gaitán S., Savić Đ., Kishimoto M., Mourão A., Lopez-Rodríguez E., Asmus D., 2023, *MNRAS*, **519**, 3237
- Tasca L. A. M., et al., 2015, *A&A*, **581**, A54
- Terrazas B. A., Bell E. F., Henriques B. M. B., White S. D. M., Cattaneo A., Woo J., 2016, *ApJ*, **830**, L12
- Terrazas B. A., Bell E. F., Woo J., Henriques B. M. B., 2017, *ApJ*, **844**, 170
- Todini P., Ferrara A., 2001, *MNRAS*, **325**, 726
- Toomre A., 1977, in Tinsley B. M., Larson Richard B. Gehret D. C., eds, *Evolution of Galaxies and Stellar Populations*. Yale Univ. Observatory New Haven, CT, p. 401
- Tremonti C. A., et al., 2004, *ApJ*, **613**, 898
- Tristram K. R. W., et al., 2022, *A&A*, **664**, A142
- Trujillo I., Graham A. W., Caon N., 2001, *MNRAS*, **326**, 869
- Trujillo I., et al., 2006, *ApJ*, **650**, 18
- Vagshette N. D., Naik S., Kumari N., Patil M. K., 2021, *Journal of Astrophysics and Astronomy*, **42**, 34
- Vasylenko A. A., Fedorova E. V., Hnatyk B. I., Zhdanov V. I., 2015, *Kinematics and Physics of Celestial Bodies*, **31**, 13
- Véron-Cetty M. P., Véron P., 2006, *A&A*, **455**, 773
- Vogelsberger M., et al., 2014, *MNRAS*, **444**, 1518
- Welch G. A., Sage L. J., 2003, *ApJ*, **584**, 260
- Werner M. W., et al., 2004, *ApJS*, **154**, 1
- Whitaker K. E., et al., 2014, *ApJ*, **795**, 104
- Willner S. P., Elvis M., Fabbiano G., Lawrence A., Ward M. J., 1985, *ApJ*, **299**, 443
- Wolf C., et al., 2009, *MNRAS*, **393**, 1302
- Wright E. L., et al., 2010, *AJ*, **140**, 1868
- Yagi M., et al., 2010, *AJ*, **140**, 1814
- Yang X., et al., 2017, *MNRAS*, **464**, L70
- Yao H. F. M., et al., 2022, *ApJ*, **939**, 26
- Yoshida M., Kawabata K. S., Ohya Y., Itoh R., Hattori T., 2019, *PASJ*, **71**, 87
- Zibetti S., Ménard B., Nestor D. B., Quider A. M., Rao S. M., Turnshek D. A., 2007, *ApJ*, **658**, 161
- da Cunha E., Charlot S., Elbaz D., 2008, *MNRAS*, **388**, 1595
- de Vaucouleurs G., de Vaucouleurs A., 1972, *Mem. RAS*, **77**, 1
- de Vaucouleurs G., de Vaucouleurs A., Corwin Herold G. J., Buta R. J., Paturel G., Fouque P., 1991, *Third Reference Catalogue of Bright Galaxies*. Springer, New York
- van Dokkum P. G., Abraham R., Merritt A., Zhang J., Geha M., Conroy C., 2015, *ApJ*, **798**, L45
- van Zee L., Haynes M. P., Salzer J. J., 1997, *AJ*, **114**, 2479
- van den Bergh S., 1976, *ApJ*, **206**, 883
- van der Wel A., et al., 2014, *ApJ*, **788**, 28

APPENDIX A: NOTES ON INDIVIDUAL GALAXIES

Some galaxies were labelled in the figures or noted in passing because they stood out for one reason or another and may, therefore, be of interest. Below are some quick comments on these galaxies.

Circinus has a significant Seyfert AGN (Tristram et al. 2022; Stalevski et al. 2023); thus, the *WISE*-determined sSFR is not applicable/correct.

NGC 1275 is the Perseus cluster’s BCG, with a substantial AGN (Burbidge & Burbidge 1965; Irwin et al. 2001). The *WISE*-determined sSFR is again not applicable/correct.

NGC 1300 is an outlying S galaxy in the $M_{\text{bh}}-M_{*,\text{sph}}$ diagram and was excluded from the Bayesian analyses for the S galaxies (Graham 2023c). It has a high Sérsic index in the $M_{*,\text{sph}}-(\text{Sérsic}, n)$ diagram (Sahu et al. 2020, their Fig. 2) and may have an unmodelled barlens component (Graham 2023a, footnote 8), but this is unlikely to increase the spheroid mass.

NGC 1316 is the Fornax cluster’s BCG. While many/most BCGs are E galaxies, this is a dusty S0 galaxy, likely built, in part,

through the acquisition of a spiral galaxy (Goudfrooij et al. 2004; Vagshette et al. 2021).

NGC 1332 is a relatively dust-free, relic compact massive galaxy without a large-scale disc (Savorgnan & Graham 2016b). It is designated an ES,b galaxy, midway between the dust-poor S0 and E galaxies. It resides in a region of the $M_{\text{bh}}-M_{*,\text{sph}}$ diagram where one finds the bulges of dusty S0 galaxies.

NGC 2787 is a reasonably dusty S0 galaxy located to the left of the $M_{\text{bh}}-M_{*,\text{sph}}$ relation for dust-poor S0 galaxies. On one hemisphere, it has strong dust rings over the inner 160 pc, and weaker dust rings out to 400 pc. It has a pseudobulge, a classical bulge (Erwin et al. 2003), a polar disc and nuclear rings that do not reside in the primary disc plane (Sil’chenko & Afanasiev 2004).

NGC 3489 is a dust-rich S0 galaxy located on the low-mass end of the dust-poor S0 sequence in the $M_{\text{bh}}-M_{*,\text{sph}}$ diagram. The measurements are not thought to be in error; instead, some outlying systems may reflect that the trends are not perfect laws of physics.

NGC 4026 comprises an old stellar population and contains no significant HI gas of its own. However, it is the dominant galaxy in its small group and has accreted a $10^8 M_{\odot}$ filament of HI gas (Welch & Sage 2003).

NGC 4342 is a tidally-stripped galaxy whose spheroid mass has been reduced by an unknown amount (Blom et al. 2014).

NGC 6251 has a Seyfert 2 AGN, a dusty nuclear disc, and a strong one-sided radio jet (Perley et al. 1984; Crane & Vernet 1997). It resides in the $M_{\text{bh}}-M_{*,\text{sph}}$ diagram, where one would expect to find BCGs. It is an E galaxy likely built from multiple major mergers but is not a BCG.

APPENDIX B: FURTHER COMMENTARY ON AGN

There are a couple of notable exceptions in Fig. 4 that warrant mention, in that they contain AGN but do not appear in the QSO/AGN box shown there. The spectacular radio galaxy, NGC 5128 (Centaurus A; Mirabel et al. 1999), has a very bright nucleus, graced by a radio-jet and Mpc-sized non-thermal radio plume, and is one of the closest AGNs. However, the host galaxy is massive and extended and contains a dusty, star-forming remnant of a past ‘wet’ merger (see Fig. 2). Consequently, the *WISE* colours are perfectly consistent with normal thermal emission, even though it is centred around a powerful non-thermal engine. In general, it has been found that galaxies may harbour a radio-quiet AGN, which is revealed, e.g., with optical spectroscopy via line ratios, but the *WISE* colours may only be sensitive to the greater host (disc + bulge populations). Yao et al. (2022) noted that if one is to comprehensively reveal AGNs in nearby galaxies, it requires a complete multi-wavelength approach, including the X-ray (nuclear activity and jets), optical (kinematics and line ratios), infrared (dust-obscured AGNs), and radio (non-thermal emission, jets and plumes). The upshot is that NGC 5128, along with NGC 1275, have nuclear (central) W1–W2 colours around 1.0, while the global or total colour is ~ 0.0 and ~ 0.1 , respectively.

Among our full sample, we recognise an additional five (along with NGC 1194 and NGC 5252) ‘warm AGN’ whose SFRs will be over-estimated to some extent. They are the spiral galaxies Circinus, NGC 1320, NGC 4151, NGC 4388 and NGC 7582. An additional three galaxies have $0.25 < (W1 - W2) < 0.4$. They are the spiral galaxies NGC 2273 and NGC 3227, along with the Perseus cluster’s BCG NGC 1275, aka Perseus A, which is an ES (elliptical) galaxy. As noted above, this type 1.5 Seyfert galaxy is initially excluded from some figures, as is Circinus, for clarity. We note that

as with NGC 5128, these “warm” galaxies have colours dominated by starlight, with only a small contribution from the AGN. When, however, we consider only the colour of the nuclear region (using an aperture set by the angular resolution of the *WISE* imaging), the resulting W1-W2 colour can be well above a value of unity, residing in the AGN/QSO region of the colour-colour diagram.

Galaxies with more captured cool gas are expected to have higher SFRs and greater AGN activity. However, as noted above, we are mindful that AGN-heated dust may interfere with some *WISE*-estimated SFRs. Focussing on the 40 S0 galaxies identified in [Graham \(2023b\)](#), five stand out in the *WISE* images for their high (non-stellar)-to-stellar mid-infrared emission level. They are the low-ionization nuclear emission-line region (LINER) dwarf galaxy NGC 404 (Seyfert: [Filippenko & Sargent 1985](#); [Willner et al. 1985](#); [Véron-Cetty & Véron 2006](#)), NGC 1194 (dusty Seyfert 1.9: [Kailey & Lebofsky 1988](#); [Véron-Cetty & Véron 2006](#); [Keel et al. 2015](#)), NGC 4594 (Sombrero galaxy with large dust disc and Seyfert 2 nucleus: [Binette 1985](#); [Filippenko & Sargent 1985](#); [Panessa & Bassani 2002](#)), NGC 5128 (Centaurus A, an unrelaxed merger with a radio jet: [Israel 1998](#)), and NGC 5252 (relic quasar / LINER / dusty Seyfert 1.9: [Huchra et al. 1982](#); [Goncalves et al. 1998](#); [Capetti et al. 2005](#); [Keel et al. 2015](#)). NGC 1194 and NGC 5252 have both been flagged above for containing a warm AGN, and they have been flagged in the literature for potentially hosting a binary black hole ([Kim et al. 2015](#); [Yang et al. 2017](#); [Vasylenko et al. 2015](#); [Fedorova et al. 2016](#)). This is unsurprising given that the higher-mass dust-rich S0 galaxies have been built from gas-rich major mergers ([Graham 2023b](#), table 2).

In addition to the above five galaxies, the strong dust lanes in the merger remnants NGC 1316 (also with a radio jet) and NGC 5018 stand out in the *WISE* images due to their red MIR colour. The only other dust-rich S0 galaxy with an SFR greater than $0.5 M_{\odot} \text{ yr}^{-1}$ is NGC 3665, and it, too, has a radio jet ([Bridle & Perley 1984](#); [Liu & Xie 1992](#); [Liu & Zhang 2002](#)). These eight galaxies have been marked in Fig. 3, and the first six are shown in Fig. 2.

The above eight S0 galaxies are dust-rich (dust=Y). Eight of the nine remaining dust-rich S0 galaxies do not have active nuclei. The exception is NGC 2974 (Seyfert 2: [Maia et al. 2003](#); [Véron-Cetty & Véron 2006](#)).

Among the four ‘dust=y’ S0 galaxies, two contain an AGN. They are NGC 2787 and NGC 3998, which contain a LINER with broad Balmer lines ([Ho et al. 1997](#); [Véron-Cetty & Véron 2006](#)). In contrast, none of the 19 ‘dust=n’ or ‘dust=N’ S0 galaxies contain an AGN according to the Activity Type in the NASA/IPAC Extragalactic Database (NED)¹⁷. This includes five ‘dust=n’ S0 galaxies, revealing that their dusty nuclear discs/rings are not powering an AGN.

For reference, among the 28 S galaxies (including Circinus), 21 contain a (predominantly Seyfert) AGN. In contrast, among the 35 remaining ETGs, 5/9 BCG (excluding the already mentioned S0 BCG NGC 1316 with its radio jet), 2/9 non-BCG ES,e, and 6/17 E contain an AGN. These 13 AGN, in 35 ETGs, consist of five Seyfert 2 nuclei, two LINERs (one with broad Balmer lines, and six Flat-Spectrum Radio Sources (FSRSs).

Another way to dice things is to report that there are 3/28 S galaxies with a radio jet or FSRS, 3/39 non-BCG S0 with a radio jet or FSRS, and 7/36 ETGs (17 E + 9 ES,e + 10 BCG) with a

radio jet or FSRS. This abundance ratio roughly represents 10 per cent for the two former galaxy types and 20 per cent for the latter.

APPENDIX C: SPECIFIC STAR FORMATION RATES

This paper has been typeset from a $\text{\TeX}/\text{\LaTeX}$ file prepared by the author.

¹⁷ <http://nedwww.ipac.caltech.edu>

Table C1. Star formation rates

Galaxy	Type	Dust	W1–W2 mag	W2–W3 mag	$\log(M_{*,\text{gal}}/M_{\odot})$ dex	SFR $M_{\odot} \text{ yr}^{-1}$
Circinus	S		0.69±0.03	4.02±0.03	10.04±0.09	4.6493±0.9689
IC 1459	E		-0.05±0.04	0.39±0.06	11.24±0.08	0.1724±0.0262
IC 2560	S		0.19±0.04	3.38±0.04	10.43±0.08	2.6410±0.2648
IC 4296	BCG (E)		-0.08±0.04	0.02±0.08	11.47±0.08	0.0994±0.0181
NGC 0224	S		-0.03±0.03	2.08±0.04	10.71±0.08	0.5871±0.0568
NGC 0253	S		0.20±0.03	3.81±0.04	10.43±0.08	3.7837±0.3807
NGC 0404	S0	Y	0.03±0.04	1.28±0.05	08.85±0.09	0.0306±0.0092
NGC 0524	S0	Y	-0.02±0.04	0.52±0.06	11.10±0.08	0.0871±0.0112
NGC 0821	ES,e		-0.04±0.04	0.27±0.13	10.64±0.08	0.0982±0.0166
NGC 1023	S0	N	-0.04±0.03	0.18±0.07	10.61±0.08	0.0182±0.0031
NGC 1097	S		0.10±0.04	3.41±0.04	11.22±0.08	15.1384±2.1432
NGC 1194	S0	Y	0.89±0.03	2.83±0.04	10.46±0.08	3.9039±0.3943
NGC 1275	BCG (ES,e)		0.32±0.04	3.00±0.04	11.52±0.09	51.7151±8.1149
NGC 1300	S		0.05±0.04	2.91±0.04	10.56±0.08	1.4286±0.1412
NGC 1316	BCG (S0)	Y	-0.03±0.04	0.65±0.05	11.43±0.08	0.2939±0.0319
NGC 1320	S		0.64±0.04	3.34±0.04	10.13±0.09	2.7987±0.2803
NGC 1332	S0 (ES,b)	n	-0.03±0.04	0.42±0.05	10.88±0.08	0.1514±0.0243
NGC 1374	S0	N	-0.06±0.04	0.12±0.07	10.33±0.08	<0.0001
NGC 1398	S		-0.00±0.04	2.14±0.04	11.17±0.08	1.9506±0.1975
NGC 1399	BCG (E)		-0.08±0.04	0.17±0.07	11.23±0.08	0.0321±0.0073
NGC 1407	E		-0.08±0.04	0.07±0.09	11.39±0.08	<0.0001
NGC 1600	E		-0.09±0.04	-0.34±0.10	11.71±0.09	<0.0006
NGC 2273	S		0.29±0.03	3.14±0.04	10.43±0.08	2.5597±0.2557
NGC 2549	S0	N	-0.05±0.03	0.33±0.06	09.97±0.08	0.0100±0.0029
NGC 2778	S0	N	-0.06±0.04	0.12±0.05	09.89±0.08	0.0154±0.0052
NGC 2787	S0	y	-0.03±0.03	0.59±0.04	09.80±0.08	0.0081±0.0021
NGC 2960	S		0.06±0.04	2.98±0.04	10.72±0.08	2.0085±0.2022
NGC 2974	S0	Y	-0.04±0.04	1.36±0.08	10.61±0.08	0.2160±0.0240
NGC 3031	S		-0.03±0.03	1.80±0.03	10.57±0.08	0.3724±0.0356
NGC 3079	S		0.24±0.03	3.64±0.04	10.41±0.08	3.6759±0.3683
NGC 3091	E		-0.03±0.04	-0.21±0.11	11.39±0.09	<0.0004
NGC 3115	ES,b	Y	-0.01±0.04	0.14±0.12	10.63±0.08	0.0108±0.0025
NGC 3227	S		0.28±0.04	3.09±0.04	10.65±0.08	3.4491±0.3488
NGC 3245	S0	n	-0.03±0.04	1.09±0.04	10.45±0.08	0.1691±0.0163
NGC 3368	S		0.04±0.04	2.13±0.04	10.55±0.08	0.5551±0.0541
NGC 3377	ES,e		-0.05±0.04	-0.09±0.08	10.13±0.08	<0.0001
NGC 3379	E		-0.08±0.04	0.12±0.05	10.64±0.08	<0.0001
NGC 3384	S0	N	-0.04±0.04	0.24±0.05	10.37±0.08	0.0334±0.0054
NGC 3414	ES,e		-0.04±0.04	0.50±0.07	10.63±0.08	0.0381±0.0049
NGC 3489	S0	Y	0.01±0.04	1.16±0.04	10.14±0.08	0.0795±0.0075
NGC 3585	ES,e		-0.05±0.04	0.06±0.09	11.03±0.09	0.0074±0.0045
NGC 3607	ES,e		-0.08±0.04	0.73±0.06	11.13±0.08	0.2514±0.0261
NGC 3608	E		-0.04±0.04	-0.13±0.10	10.56±0.09	<0.0001
NGC 3627	S		0.11±0.04	3.44±0.04	10.63±0.08	3.6944±0.3702
NGC 3665	S0	Y	-0.05±0.04	1.33±0.04	11.13±0.08	0.7200±0.0709
NGC 3842	BCG (E)		-0.08±0.06	-0.43±0.07	11.45±0.09	<0.0009
NGC 3923	E		-0.10±0.04	-0.03±0.08	11.30±0.08	<0.0001
NGC 3998	S0	y	-0.00±0.04	1.39±0.05	10.30±0.08	0.1304±0.0127
NGC 4026	S0	y	-0.04±0.03	0.52±0.05	10.18±0.08	0.0009±0.0008
NGC 4151	S		0.79±0.04	2.82±0.04	10.53±0.08	4.3674±0.4406
NGC 4258	S		0.04±0.04	2.44±0.04	10.56±0.08	0.9339±0.0918
NGC 4261	E		-0.08±0.04	0.22±0.08	11.17±0.08	0.1530±0.0231
NGC 4291	E		0.01±0.04	0.00±0.09	10.47±0.08	<0.0001
NGC 4303	S		0.15±0.04	3.87±0.04	10.71±0.09	7.0129±0.8237
NGC 4339	S0	N	-0.08±0.04	0.67±0.14	10.02±0.08	0.0728±0.0160
NGC 4342	S0	N	-0.07±0.04	0.31±0.04	10.10±0.08	<0.0001
NGC 4350	S0	n	-0.06±0.04	0.51±0.06	10.35±0.08	0.0198±0.0028
NGC 4371	S0	n	-0.03±0.04	0.64±0.09	10.38±0.08	0.0227±0.0041
NGC 4374	E		-0.03±0.04	-0.04±0.07	11.14±0.08	<0.0001
NGC 4388	S		0.43±0.04	3.15±0.04	10.12±0.08	1.8543±0.1848
NGC 4395	S		0.08±0.07	2.20±0.12	09.03±0.09	0.1345±0.0347
NGC 4429	S0	Y	-0.04±0.04	0.86±0.05	10.75±0.08	0.1446±0.0146
NGC 4434	S0	N	-0.04±0.04	-0.00±0.06	10.03±0.08	<0.0001

Table C1. Continued

Galaxy	Type	Dust	W1–W2 mag	W2–W3 mag	$\log(M_{*,\text{gal}}/M_{\odot})$ dex	SFR $M_{\odot} \text{ yr}^{-1}$
NGC 4459	S0	Y	-0.02±0.04	1.17±0.10	10.56±0.08	0.2756±0.0299
NGC 4472	BCG (E)		-0.09±0.04	0.28±0.12	11.41±0.08	0.2140±0.0271
NGC 4473	ES,e		-0.06±0.04	0.15±0.08	10.53±0.08	0.0303±0.0049
NGC 4486	BCG (E)		-0.07±0.04	0.33±0.05	11.31±0.08	0.1950±0.0294
NGC 4501	S		0.06±0.04	3.05±0.04	10.89±0.08	3.4779±0.3495
NGC 4526	S0	Y	-0.03±0.04	1.14±0.05	10.84±0.08	0.2872±0.0281
NGC 4552	ES,e		-0.07±0.04	0.50±0.10	10.77±0.09	0.0448±0.0065
NGC 4564	S0	N	-0.04±0.04	0.31±0.05	10.12±0.08	0.0038±0.0009
NGC 4578	S0	N	-0.07±0.04	-0.24±0.10	10.05±0.08	<0.0001
NGC 4594	S0	Y	-0.02±0.04	0.90±0.05	11.06±0.08	0.3270±0.0325
NGC 4596	S0	Y	-0.00±0.04	0.34±0.08	10.54±0.08	0.0500±0.0057
NGC 4621	ES,e		-0.09±0.04	0.42±0.13	10.89±0.08	0.1176±0.0146
NGC 4649	E		-0.07±0.04	0.42±0.10	11.24±0.08	0.1649±0.0190
NGC 4697	ES,e		-0.05±0.04	0.09±0.06	10.65±0.08	0.0347±0.0057
NGC 4699	S		-0.00±0.04	2.20±0.04	11.06±0.08	1.5938±0.1583
NGC 4736	S		0.02±0.04	2.71±0.04	10.38±0.08	0.8263±0.0802
NGC 4742	S0	N	-0.02±0.04	0.40±0.05	09.99±0.08	0.0158±0.0044
NGC 4762	S0	N	-0.04±0.04	0.18±0.07	10.56±0.08	<0.0001
NGC 4826	S		0.02±0.04	2.21±0.04	10.54±0.08	0.7212±0.0698
NGC 4889	BCG (E)		-0.07±0.04	-0.17±0.09	11.72±0.09	<0.0010
NGC 4945	S		0.20±0.03	3.56±0.03	10.23±0.08	2.0911±0.2064
NGC 5018	S0	Y	0.03±0.04	0.89±0.07	11.10±0.08	0.4968±0.0514
NGC 5077	E		-0.06±0.04	0.22±0.07	11.02±0.08	0.1213±0.0188
NGC 5128	S0	Y	0.02±0.03	2.53±0.03	10.86±0.08	1.7869±0.1759
NGC 5252	S0	Y	0.58±0.04	2.27±0.04	11.05±0.08	5.6485±0.6099
NGC 5419	BCG (E)		-0.09±0.04	0.04±0.12	11.64±0.08	0.1488±0.0284
NGC 5576	E		-0.03±0.04	-0.23±0.05	10.70±0.08	<0.0001
NGC 5813	S0	y	-0.04±0.04	0.03±0.12	11.10±0.08	0.0403±0.0080
NGC 5845	ES,b	n	-0.04±0.04	0.53±0.04	10.14±0.08	0.0247±0.0040
NGC 5846	E		-0.07±0.04	-0.13±0.08	11.18±0.09	<0.0001
NGC 6251	E		-0.04±0.04	1.05±0.04	11.51±0.08	1.0416±0.1047
NGC 6861	ES,b	Y	-0.04±0.04	0.76±0.05	10.84±0.08	0.1063±0.0112
NGC 6926	S		0.19±0.03	3.79±0.04	11.08±0.08	19.2827±2.9770
NGC 7052	E		-0.06±0.04	0.58±0.05	11.22±0.08	0.3386±0.0463
NGC 7332	S0	N	-0.04±0.04	0.46±0.05	10.48±0.08	0.0497±0.0083
NGC 7457	S0	N	-0.03±0.04	0.27±0.11	09.92±0.08	0.0150±0.0040
NGC 7582	S		0.59±0.03	3.29±0.04	10.59±0.08	8.9545±1.0156
NGC 7619	E		-0.08±0.04	-0.01±0.12	11.29±0.08	<0.0003
NGC 7768	BCG (E)		-0.10±0.04	-0.38±0.05	11.44±0.09	<0.0013
UGC 3789	S		0.09±0.03	3.22±0.04	10.51±0.08	2.0713±0.2073

Column 2: Galaxy type (Graham & Sahu 2023a,b). Following Graham (2023b), NGC 4594 and NGC 2974 are considered S0 galaxies rather than S galaxies. The four ES,b galaxies noted there continue to be counted here among the S0 galaxies. NGC 4395 and NGC 6926 are bulge-less S galaxies. Column 3: Dust ‘bin’ for the S0 galaxies (taken from Graham 2023b). Y = Strong Yes, y = weak yes, n = nuclear dust, N = No dust (see Section 2). Columns 4 & 5: *WISE* colours. The W1, W2, W3 and W4 passbands are centred at 3.368, 4.618, 12.082 and 22.194 μm , respectively. Column 6: Logarithm of the galaxies’ stellar mass derived from *WISE* photometry using a Chabrier (2003) IMF. (For Fig. 1, 0.05 dex was subtracted from these values to create consistency with the Kroupa (2002) IMF. For Fig. 3, no adjustment was made. For the other figures, and the derivation of the sSFRs, the stellar masses from Graham & Sahu (2023a) were used.) Column 7: Star formation rate in units of solar mass per year.